UNIVERSITÀ DEGLI STUDI DI PADOVA

Dipartimento di Fisica e Astronomia "Galileo Galilei"

Corso di Laurea in Fisica

Tesi di Laurea

Misure di vita media negli isotopi di Hg poveri di neutroni utilizzando il metodo Recoil Distance Doppler Shift

Lifetime measurements in neutron-deficient Hg isotopes using the Recoil Distance Doppler Shift method

Relatori

Dr. José Javier Valiente Dobón

Dr. Irene Zanon

Laureando

Stefano Semeraro

Anno Accademico 2022/2023

Abstract

La catena isotopica del mercurio è caratterizzata da numerosi fenomeni relativi all'evoluzione della forma nucleare, come lo shape-staggering tra nuclei di masse dispari e pari, e la comparsa di coesistenza di forma. Questi fenomeni forniscono informazioni utili sull'evoluzione della struttura nucleare nella regione dei nuclei pesanti nella tavola di Segré. Un esperimento volto a studiare gli stati eccitati del ^{188}Hg è stato svolto ai Laboratori Nazionali di Legnaro usando una reazione di fusione-evaporazione, utilizzando un fascio di ^{34}S su un bersaglio di ^{160}Gd. Nella stessa reazione è stato popolato anche il nucleo ^{189}Hg, di cui sono ancora ignote numerose proprietà spettroscopiche, tra cui le vite medie degli stati eccitati.

I raggi γ emessi dalla diseccitazione dei nuclei sono stati studiati usando l'array di rivelatori al germanio iperpuro GALILEO accoppiato a Neutron Wall, un array di scintillatori liquidi, e il plunger, un dispositivo utilizzato per le misure di vita media di stati eccitati dell'ordine dei picosecondi. Uno studio della spettroscopia del nucleo è stato svolto e due nuove transizioni gamma sono state aggiunte allo schema dei livelli noto finora. Inoltre, le vite medie di due stati eccitati a bassa energia del ^{189}Hg sono state misurate usando il metodo Recoil Distance Doppler Shift. Dalle vite medie di questi due stati, finora ignote in letteratura, sono state estratte le probabilità di transizione ridotta e del confronto tra queste ultime e le stime di Weisskopf è stato possibile fornire un'interpretazione sulla natura dei primi due stati eccitati del ^{189}Hg.

Contents

Introduction

A previous study of the ^{188}Hg isotope was performed at Laboratori Nazionali di Legnaro (LNL) in 2018 [1], with the aim of studying the presence of nuclear shape coexistence in this nucleus. The experiment was performed in 2016 with the GALILEO (Gamma Array of Legnaro INFN Laboratories for nuclEar spectrOscopy) array, installed at LNL at the time of the experiment.
The aim of this thesis is to continue the analysis of these data, focusing on the ^{189}Hg isotope, the second most populated during the reaction used for the experiment. This nucleus is of particular interest because the study of neutron-deficient nuclei from the region with the proton number just below the shell closure (Z=82), such as Hg isotopes, could provide interesting information about shape coexistence, and the interplay between collective and individual degrees of freedom [2]. The present thesis will focus on γ-spectroscopy and the measurements of lifetimes of excited states in the range of picoseconds, still unknown in literature. In addition, the study of even-odd nuclei could give some interesting theoretical interpretations.

Interest in studying odd-even nuclei

The high-mass neutron-deficient region of the Segré chart is of high interest and widely researched. In particular, Hg, Pb and Po isotopes are very helpful for deeper understanding collective phenomena, such as shape coexistence.

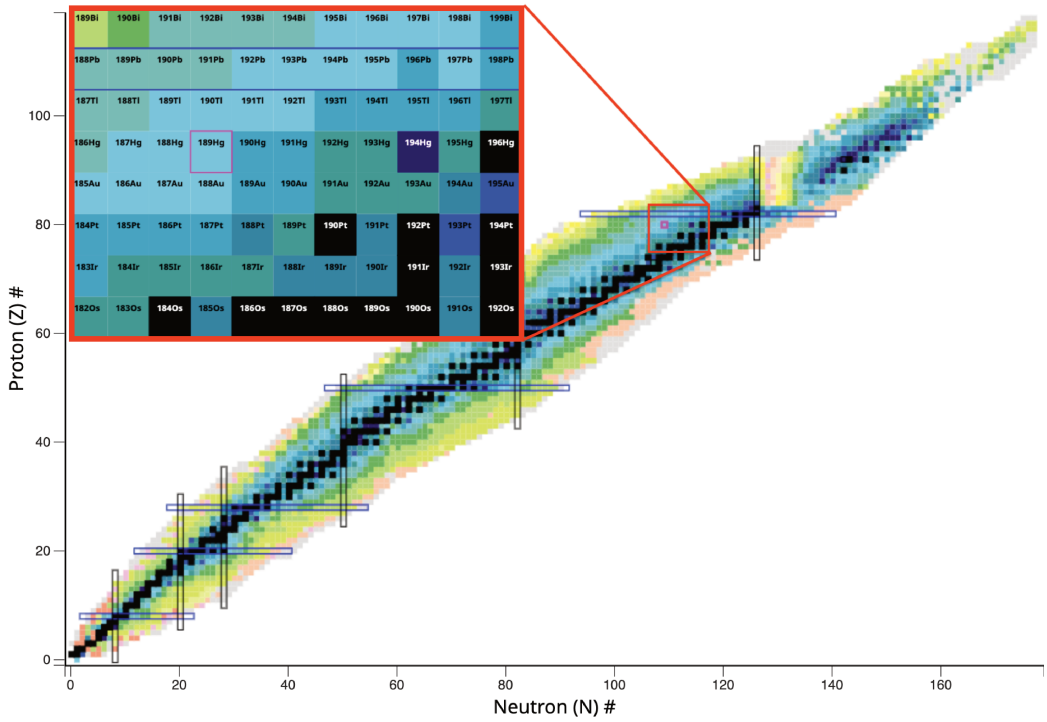

Figure 1: The Segré chart, with a focus on the neutron-deficient region. In pink, ^{189}Hg, the nucleus of interest. Figure adapted from [3].

Over the years, most of the studies were performed on even-even nuclei, because they are easier to

analyse thanks to their symmetric properties, and can be described with simpler theoretical models, while even-odd nuclei are more complicated, because of the presence of one uncoupled nucleon. For this reason, the study for these latter nuclei was focused mainly on bulk properties, such as mass and charge radius measurements, and spectroscopy. The aim of this thesis is to study some of the spectroscopic properties of ^{189}Hg (Z=80, N=109) and to measure the lifetime of two excited states, in order to deeper understand the behaviour of this nucleus. An example of the unconventional behaviour of odd-even nuclei is reported in Figure 2, where the trend for charge radius measurements for Hg and Pb isotopes is reported. In Hg isotopes, for lower number of neutrons, it can be noticed a staggering in the values of the radius: the values of the charge radius increases for odd masses, while for even masses the values follow the same trend observed for heavier Hg isotopes. On the basis of Monte Carlo Shell Model considerations, odd-mass deformed nuclei are expected to have larger radii. This is because the strongly deformed state, combined with monopole and quadrupole effects, lead to shape staggering phenomena. In the middle of the shell (such as for $^{181-185}$Hg) the odd isotopes are then more deformed than the even ones [4]. For higher values of N, this phenomena becomes secondary, leading to a monotone trend of the radius as a function of the neutron number. This is also the case for Pb isotopes (Z=82, magic number of protons), where this staggering is not observed. The presence of radius staggering is considered as one of the main hint for the presence of shape coexistence phenomena, even if it is not a necessary condition. For example, shape coexistence is present also in nuclei with no radius staggering, such as ^{188}Hg [1] or various Pb isotopes.

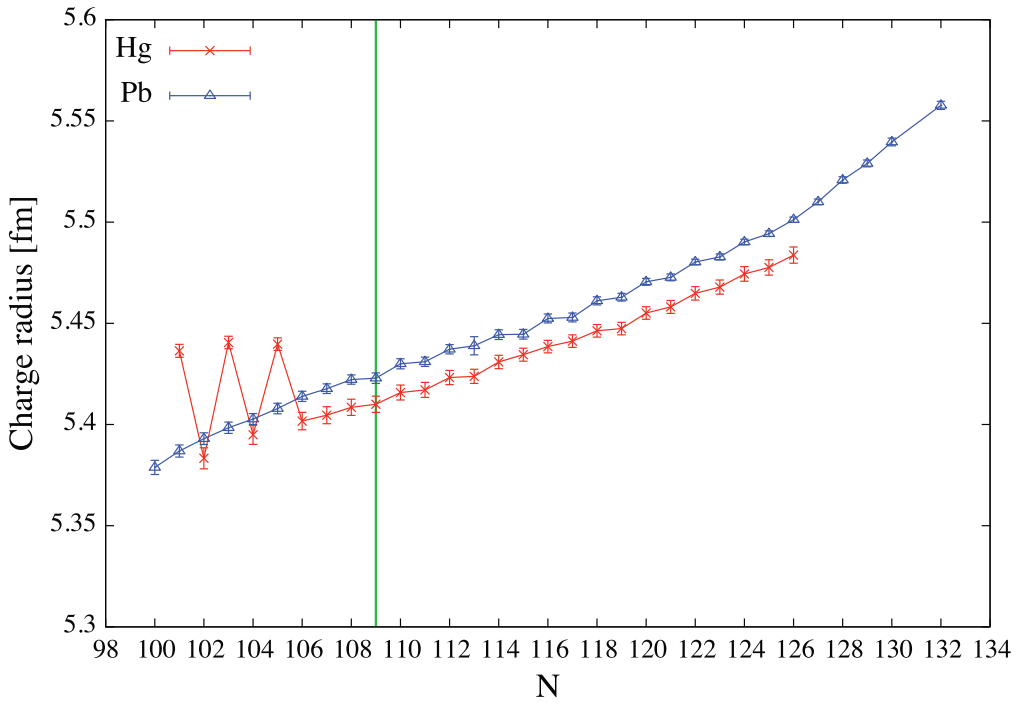

Figure 2: Charge radius trend for Hg and Pb isotopes. In green, the number of neutrons (N=109) of the nucleus of interest, ^{189}Hg. The staggering of the data at low values of N for Hg can be explained by null contribution of the coupling term in the binding energy of the nucleus. This phenomenon is a hint for the presence of shape coexistence. At higher values of N, this phenomena becomes less relevant, leading to a monotone trend of the data. Data taken from [5].

This type of nuclei are far from the valley of stability and for this reason are difficult to populate. One efficient way to populate nuclei in this region are fusion-evaporation reactions, explained in the following section.

Fusion-evaporation reactions

A way to populate the neutron-deficient region is via fusion-evaporation reactions. This type of reactions is useful to perform spectroscopy studies because it populates the high-energy, high-spin

states of the nucleus. Nevertheless, the presence of isomers could restrict the analysis only on the levels lying above of these states. That is the case of the $\frac{13}{2}^+$ level of ^{189}Hg.
In-beam reactions can be classified through some parameters, such as the energy of the beam or the impact parameter b: when b is large, the nuclei involved in the reaction are mainly subject to Coulomb force and elastic scattering is observed, such as in Rutherford scattering and Coulomb excitation; at smaller values of b, the nuclei have the energy necessary to overcome the Coulomb barrier, and start to be subject also to nuclear forces. If the energy of the beam is sufficiently high, the impact parameter becomes very small and the two nuclei completely overlap, leading to fusion-fission and fusion-evaporation reactions.
Fusion-evaporation reactions are caused by a strong overlap of the distributions of the projectile and the target nuclei. If the energy of the compound nuclei is high enough, it can lead to the fission of the latter; otherwise, the fusion of the nuclei brings to the formation of a highly-excited compound nucleus. Its de-excitation occurs through the evaporation of particles, such as protons, neutrons or alphas. The evaporation residue will be again in a highly-excited state. At this moment, the γ decay becomes the dominant de-excitation mode. During the reaction we can then directly populate a wide range of high-spin states, which will then decay to lower-spin states, until they reach the ground state. In order to discriminate between Coulomb excitation and fusion-evaporation reactions, the ancillary array Neutron Wall (see section 1.3) has been coulped to GALILEO. A scheme of the fusion-evaporation process is reported in Figure 3.

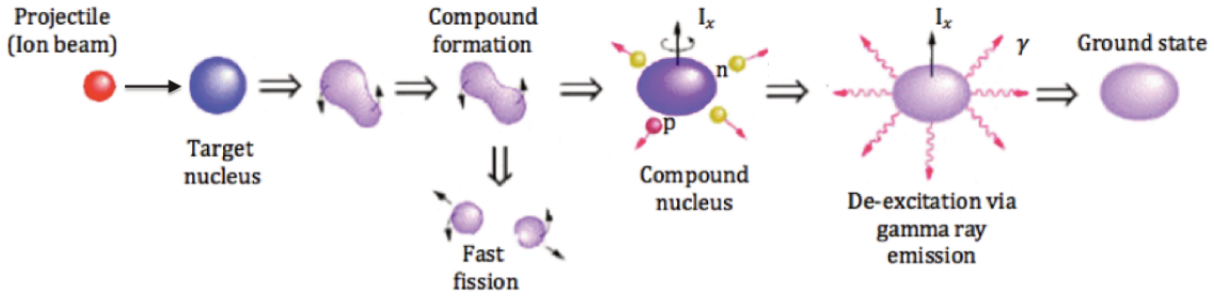

Figure 3: A schematic representation of a fusion-evaporation reaction.

γ decay

A γ decay consists in the emission of a γ ray from an excited nucleus. It is described by

$$^A_Z X^* \rightarrow ^A_Z X + \gamma$$

where X is a generic nucleus and the star represents a generic excited state of the nucleus. The γ decay does not change the isotopic nature of the nucleus.
The spectrum of the γ decay is discrete, and the energy of the photons emitted vary in a range going from 0.1 to 10 MeV. From energy and momentum conservation, we can express the difference of energy between the two levels as

$$\Delta E = E_\gamma + \frac{E_\gamma^2}{2Mc^2}$$

where E_γ is the energy of the photon emitted, M is the mass of the nucleus and c the velocity of light in vacuum. Because of the great difference between ΔE $(= O(MeV))$ and the energy at rest of the nucleus Mc^2 $(= O(100GeV))$, we can do a second order Taylor expansion:

$$E_\gamma = Mc^2 \left[-1 + \sqrt{1 + \frac{2\Delta E}{Mc^2}} \right] \simeq \Delta E - \frac{(\Delta E)^2}{2Mc^2}$$

The second term is of the order of eV, so it is negligible. Therefore, we can not consider the recoil of the nucleus and conclude that the energy of the γ ray emitted is equal to the energy gap between the initial excited state and the final state:

$$E_\gamma = \Delta E$$

Electromagnetic radiation corresponds to the propagation of oscillating electric and magnetic fields, mutually orthogonal, and its evolution is described by Maxwell equations. We can classify γ-radiation in two types, based on the origin of the radiation: electric transitions (E), caused by an oscillating distribution of charge, and magnetic transitions (M), caused by an oscillating magnetic moment.
These transitions are then governed by the conservation of the angular momentum

$$|I_i - I_f| \leq L \leq |I_i + I_f|$$

with I_i and I_f being the initial and final angular momentum, respectively, and L the angular momentum of the emitted photon. γ-transitions are then classified also by the value of the multipole order L: $L = 1$ are dipole transitions, $L = 2$ are quadrupole transitions, and so on.
An electromagnetic transition is then uniquely identified by the type of the transition (σ=E, B) and its multipolarity (L=1, 2, 3, etc.). At the same value of L, electric transitions are 100-1000 times more probable than magnetic transitions; at the same type of the transition σ, the probability of a transition corresponding to a certain value of L is $O(10^4)$ more probable than the one corresponding to the next value of multipolarity $L + 1$. No L=0 γ-transitions can be observed, due to the non-null value of the photon spin (S=1).

Gamma-matter interaction

In order to build γ-ray detectors, it is essential to study how electromagnetic radiation interacts with matter. There are three main phenomena, each dominant in a certain energy range: the photoelectric effect, the Compton scattering and the production of particle-antiparticle pairs.
The photoelectric effects consists in the absorption of an incident photon of an atom, and the consequent ejection of an electron, called photoelectron, belonging to one of the electronic shells of the atom. This electron is bounded to the atom by a certain binding energy B_e, depending on the shell of the emitted electron: external shells will have lower values of B_e, while internal shells will have a higher value. The photoelectric effect has then a threshold energy, corresponding to the binding energy. If the energy of the photon is lower than B_e, the phenomenon will not occur. As can be seen from Figure 4, the mass absorption coefficient (proportional to the probability of the effect to occur) has a discontinuous trend: the peaks correspond, in fact, to the binding energy of every internal shell. The electron will then be ejected with a kinetic energy equal to

$$T_e = E_\gamma - B_e \simeq E_\gamma$$

where the last equality is because binding energies are usually of the order of $O(10eV)$, while we work with γ rays with energy going from hundreds of keV to tens of MeV. Photoelectric effect is predominant for energies going from tens of eV to hundreds of keV.
The Compton scattering consists in the elastic collision between an incident photon and an electron belonging to an atom. The photon will then be scattered with a deviation angle θ with respect to the motion axis, and will transfer part of its energy to the electron, which will be ejected from the atom. The energy of the scattered photon will be given by

$$E'_\gamma = \frac{E_\gamma}{1 + \frac{E_\gamma}{mc^2}(1 - cos\theta)}$$

where E_γ and E'_γ are the energies of the incident and scattered photon, respectively, m is the mass of the electron and θ is the scattering angle. Compton scattering is dominant for energies going from hundreds of keV to some MeV.
Pair production consists in a photon transforming in a particle-antiparticle pair, typically electron-positron. This is due to the pairing of the oscillating electric field of the photon with the electric field generated from a nearby nucleus. The threshold energy for pair production will then be the sum of the rest energy of the products, namely

$$E_\gamma \geq 2mc^2 \simeq 1.022MeV$$

where E_γ is the energy of the photon and m is the mass of the electron. Each the electron and the positron will then have same energy, equal to

$$E_e = \frac{E_\gamma - 2mc^2}{2}$$

The positron, being antimatter, will then annihilate with another electron, generating a couple of photons, each with an energy of $E'_\gamma = 511keV$. The complete process can then be described as

$$\gamma \rightarrow e^- e^+ \qquad e^- e^+ \rightarrow \gamma\gamma$$

Pair production is dominant for energies higher than 4-5 MeV.
The intensity of a photon beam, such as the number of incident photons, impinging on a specific material, decreases exponentially, following the law

$$I(x) = I_0 e^{-\mu x}$$

where x is the distance covered by the photon and μ is defined as the linear absorption coefficient ($[m^{-1}]$), and is specific for every material. The coefficient μ is proportional to the cross-section σ, and then to the probability of the reaction to happen. This coefficient will then be the sum of the contributes given by the three processes of reaction with matter:

$$\mu = \mu_{pe} + \mu_C + \mu_{pp}$$

where the three addends are the linear absorption coefficients for photoelectric effect, Compton scattering and pair-production, respectively. Similarly, it can be defined the mass absorption coefficient as

$$\mu_{mass} = \frac{\mu}{\rho} \qquad \left[\frac{cm^2}{g}\right]$$

where ρ is the density of the material. The exponential law then becomes

$$I(d) = I_0 E^{-\mu_{mass} d} \quad with \quad d = \rho x$$

The study of the mass absorption coefficient as a function of the energy of the photon is essential to build detectors. An example for germanium, used for γ-detection in the GALILEO array, is reported in Figure 4. It can be seen that in the region of interest for this study, going from hundreds of keV to some MeV, Compton scattering is the dominant effect. Compared to Compton scattering, photoelectric effect provides a higher energy resolution. This is because, in the latter, the total energy of the photon is completely absorbed by the photoelectron, which energy can be measured more precisely. Taking into account a great amount of Compton events would lead to a great decrease in energy resolution of the detector. For this reason, eight anti-Compton shields will be coupled to every germanium detector of GALILEO (see section 1.2.2). This will increase the resolution of the detectors, at the cost of a great loss in statistics.
A new generation HPGe array, AGATA, has been recently moved to LNL and has been operational since 2022. The AGATA array allows one to reconstruct the trajectory of the photon with a precision of some mm [7]. This also permits to discriminate among Compton scattering and other types of events. Compared to GALILEO, then, it has a better angular resolution, a higher energy resolution and a higher efficiency. This new detector allows for the study of more exotic nuclei and more experimentally challenging properties of excited nuclear states.

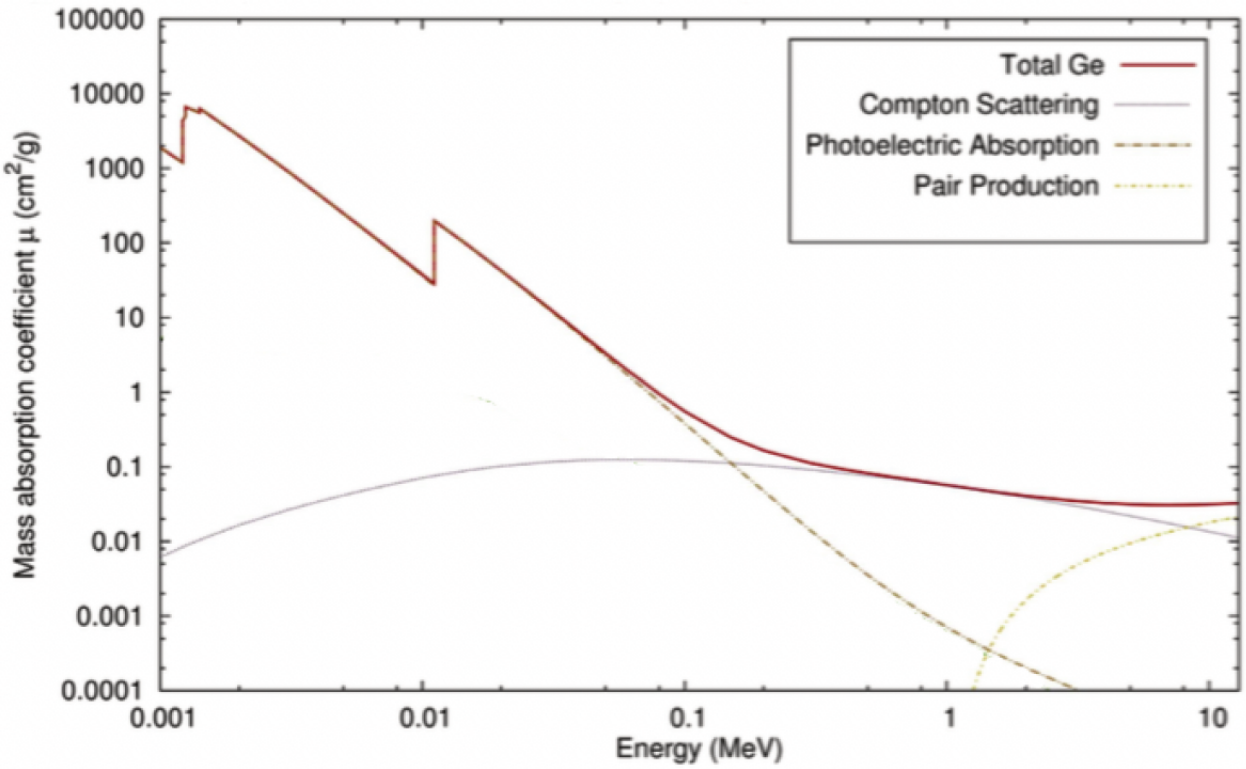

Figure 4: Mass absorption coefficient for germanium as a function of the energy, for different interaction modes. Figure taken from [6].

Experimental Apparatus

Excited states in neutron-deficient nuclei can be populated in fusion–evaporation reactions utilizing high-energy stable beams. The principal aim of the experiment was to study ^{188}Hg, so the used fusion-evaporation reaction was optimized to populate the nucleus of interest. A ^{34}S beam at the energy of 185 MeV impinged onto 600 $\mu g/cm^2$ target of ^{160}Gd (2.5 mg/cm^2 thick ^{181}Ta fronting) with the evaporation of 6 neutrons. To have cleaner data, the ancillary array Neutron Wall (further discussed in section 1.3) was coupled to the GALILEO array, in order to discriminate the events in coincidence with one or more detected neutrons [6]. The following table shows the main nuclei populated in the reaction and their respective yields:

Z	N	nucleus	yields [%]
80	108	^{188}Hg	63.7 %
80	109	^{189}Hg	18.5 %
79	109	^{188}Au	4.23 %
78	108	^{186}Pt	3.79 %
79	110	^{189}Au	3.27 %
78	107	^{185}Pt	2.67 %
80	110	^{190}Hg	0.94 %
		other	2.9 %

Table 1.1: The main nuclei populated during the fusion-evaporation reaction.

The aim of this thesis is to study the low-lying states of ^{189}Hg, the second most populated nucleus during the reaction. The lower population of this isotope leads to more inaccuracies in the results, caused by the lower statistic. More accurate measurements could be made optimizing the fusion-evaporation reaction for ^{189}Hg.

1.1. Accelerators

Two different accelerators were used to accelerate the stable beam of ^{34}S at the energy required for the reaction: the XTU-Tandem and the ALPI linear accelerator.

1.1.1. The XTU-Tandem accelerator

The XTU-Tandem is an electrostatic accelerator for stable beams. The ion source is placed upstream, and injects negative-charged ions in the accelerating pipe. The ions will be then accelerated by a high-voltage terminal, placed in the middle of the tube, which can reach a maximum of 14.5 MV of voltage. The terminal is charged by two ladderton. In the terminal, the ions pass through a thin carbon foil, called 'ion stripper', which has the aim to remove a great number of electrons; the ions are then highly positive-charged, and so accelerated by the same terminal to the opposite end of the accelerating pipe. The beam can then be addressed to the experimental areas, or it can be bent by magnets located at the end of the XTU-Tandem and injected to ALPI for the post-acceleration.

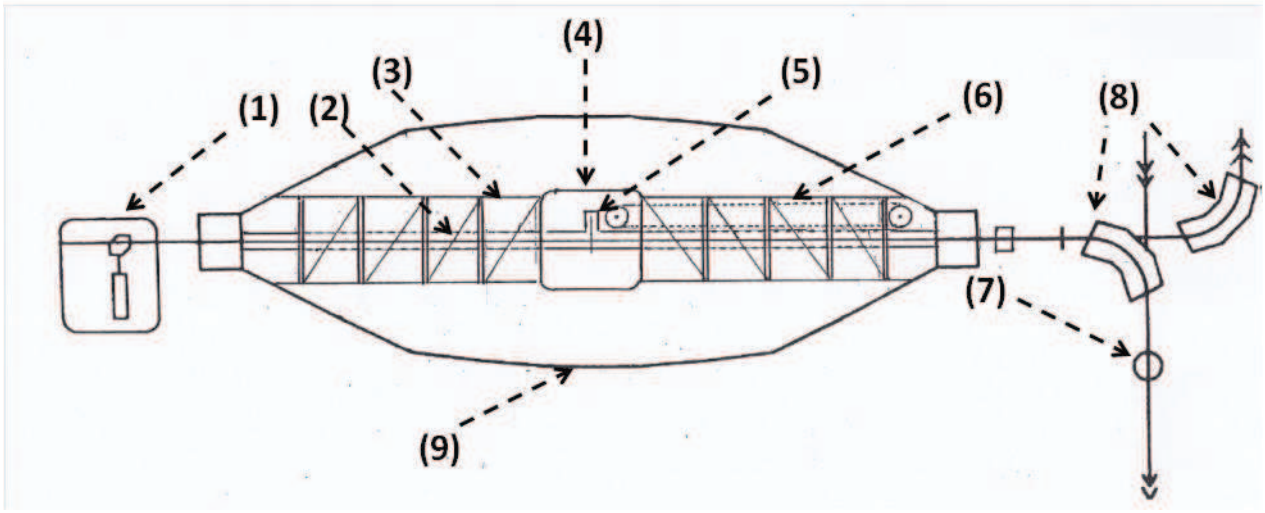

Figure 1.5: Scheme of the XTU-Tandem. The numbers correspond to: (1) the ion source; (2) the accelerating pipe; (3) the column which supports the (4) high voltage terminal, inside of which is located (5) the ion beam stripping station; (6) the 'ladderton'; (7) the beam diagnostic station; (8) bending magnets; (9) the tank filled with SF_6 gas at 7 atm. Figure taken from [8].

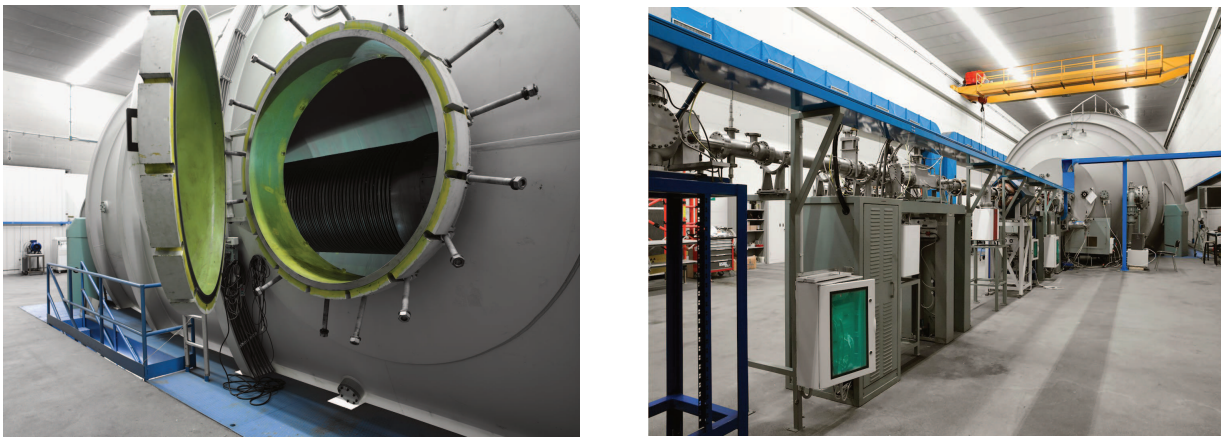

Figure 1.6: On the left, a picture of the Tandem tank, in which can be seen the beam tube and the voltage terminal; on the right, a picture of the final stretch of the accelerator, where the beam is injected in the switching magnets. Pictures taken from [8].

1.1.2. The ALPI linear accelerator

ALPI is a radio-frequency linear accelerator working in the superconductive regime, in order to reduce costs in operating and reach higher electromagnetic fields. ALPI cavities are made of niobium in contact with a bath of liquid helium (T=9.2 K); these cavities are grouped into sets of 4 cryostats, which can isolate the supercold cavities from the external environment. The accelerating cavities are of the QWR (Quarter Wave Resonator) type. A buncher, operating at 80 MHz, provides the bunch structure necessary for the acceleration in the oscillating electric field. ALPI has three different section, corresponding to different velocity regimes: one at low-β (β=0.055, 24 cavities), one at medium-β (β=0.11, 14 cavities) and one at high-β (β=0.14, 24 cavities). After the acceleration, the beam is directed to the experimental halls.

1.2. GALILEO spectrometer

GALILEO is an array for advanced in-beam γ-ray spectroscopy, installed at the Legnaro National Laboratories at the time of the experiment (2016). It consisted of 25 high-purity germanium (HPGe) detectors, positioned in rings at 152° (5 detectors), 129° (5 detectors), 119° (5 detectors) and 90° (10 detectors) with respect to the beam axis. Each of these detectors is equipped with eight bismuth

Figure 1.7: On the left, a picture of ALPI and the cryostats; on the right, the interior of a cryostat. Pictures taken from [8].

germanate crystals, used as anti-Compton shields, in order to reject Compton-scattering events.
A new phase of GALILEO was realized in the years after the experiment, adding 10 triple cluster detectors in forward angle with respect to the beam, increasing its efficiency and solid angle coverage. Thanks to its particular design, a wide variety of ancillary detectors can be coupled to GALILEO, in order to improve its sensitivity and discriminate between various physical phenomena. During this experiment, the ancillary detector Neutron Wall was coupled to GALILEO, for neutron-γ discrimination.
The GALILEO array was designed to maximise the photo-peak efficiency under typical in-beam medium-high γ ray multiplicity, thanks to its symmetric geometry with respect to the beam. In particular, during this experiment, the total photo-peak efficiency at 1332 keV was $\epsilon \sim 2.4\%$.

1.2.1. HPGe

For the γ-detection in the GALILEO array, high-purity germanium crystals have been used, characterized by an excellent energy resolution. The level of impurity in HPGe is very low, with a rate of about one impurity every 10^{12} atoms. Germanium detectors are optimal for γ-spectroscopy, where the energy range of the photons varies from 10 keV to few MeV.
The conduction mechanism is very different from a material to another. There are three energy bands: the valence band (VB), at lower energy, where electrons are bounded to the atom; the conduction band (CB), at higher energy, in which electrons are free to move and shared with the other atoms in the lattice; and a forbidden band between these two, at middle energy. Semiconductors, such as silicon and germanium, are characterized by a small band gap between VB and CB. When the radiation impinges on the crystal, gives energy to the electron in the VB, promoting it to the CB and generating an electron-hole pair. The typical energy gap for silicon detectors is 1.2 eV, while for germanium detectors is 0.7 eV. For this reason, the latter are more sensible to radiation, and have better energy resolution. However, the thermal energy at room temperature is high enough to promote some of the electrons in the CB, affecting the measurement. It is then necessary to keep the crystal tempertaure between 77 K and 90 K.

1.2.2. Anti-Compton shields

To reject Compton-scattering events, each of the HPGe detectors is surrounded by eight optically isolated bismuth germanate (BGO) crystals. BGO crystals are inorganic scintillators, which have the property to emit visible light when ionizing radiation (in this case, γ rays) passes through it.
An event is rejected when it is detected by a BGO in coincidence (90 ns) with an event detected

in HPGe. This procedure has the aim to discard all of the detected events that do not contain the complete information on the energy of the photon. In fact, if a BGO detects an event, it means that the photon did not lose all of its energy inside the HPGe, but scattered outside of it.
This procedure permits us to increase the P/T of about 50%, though affecting the geometric efficiency of the array, since the application of BGO crystals on every HPGe limits the solid angle coverage.

1.2.3. Pre-sorting of experimental data

An energy calibration of each of the 25 HPGe detector is necessary, in order to convert the ADC channels to the corresponding real energy, measured in keV. The calibration has been done with seven different γ-sources, reported in Table 1.2, whose peaks are well known.

Source	Energy range [keV]	Activity (21/07/16) [kBq]
^{60}Co	1173 - 1332	327 ± 9
^{137}Cs	661	369 ± 11
^{133}Ba	81 - 384	370 ± 11
^{22}Na	511 - 1274	286 ± 8
^{54}Mn	835	167 ± 5
^{88}Y	898 - 1836	23.8 ± 0.7
^{152}Eu	122 - 1408	307 ± 9

Table 1.2: γ-sources used for the energy calibration of GALILEO, with the respective energy ranges and activity of the γ-source. The activities were measured the day in which the calibration was done.

The centroid of each peak has been extracted from the raw spectra via gaussian fit, and a linear regression has been done to extract the parameters of the calibration, as shown in Figure 1.8.

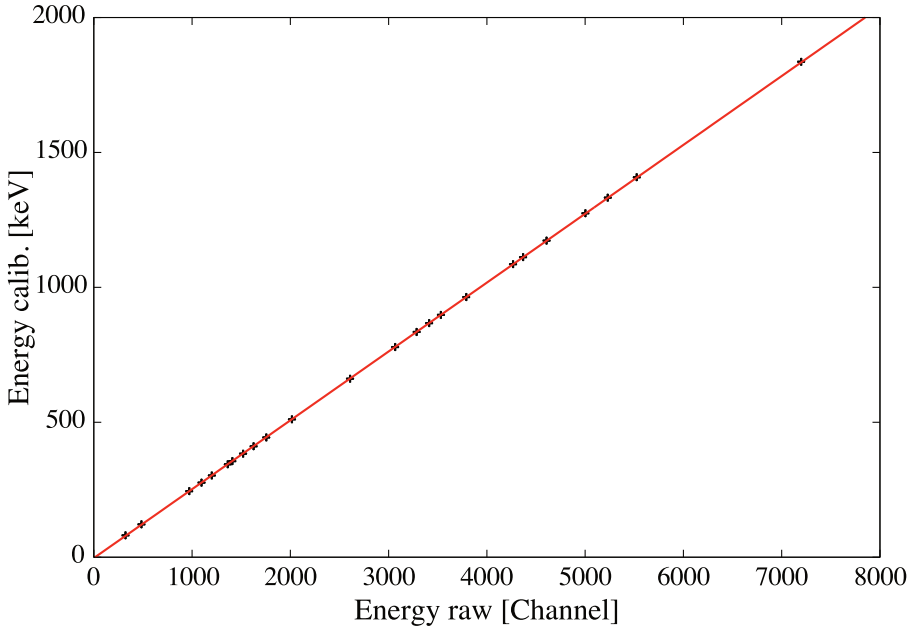

Figure 1.8: Calibrated energy as a function of the raw energy, for detector SC07. The fitted calibration function is linear.

One of the most important feature of HPGe detectors, and the main reason for their wide use in γ-spectroscopy, is the high energy resolution, especially compared to other types of detectors, such as silicon ones or scintillators. The resolution is evaluated through the measurement of the full-width at half maximum (FWHM) value of the peaks.
The dependence of FWHM from the energy is expressed by the empirical expression:

$$FWHM = \sqrt{a + bE_\gamma + cE_\gamma^2} \tag{1.1}$$

with a, b, c fitting parameters. The experimental data are shown in Figure 1.9.

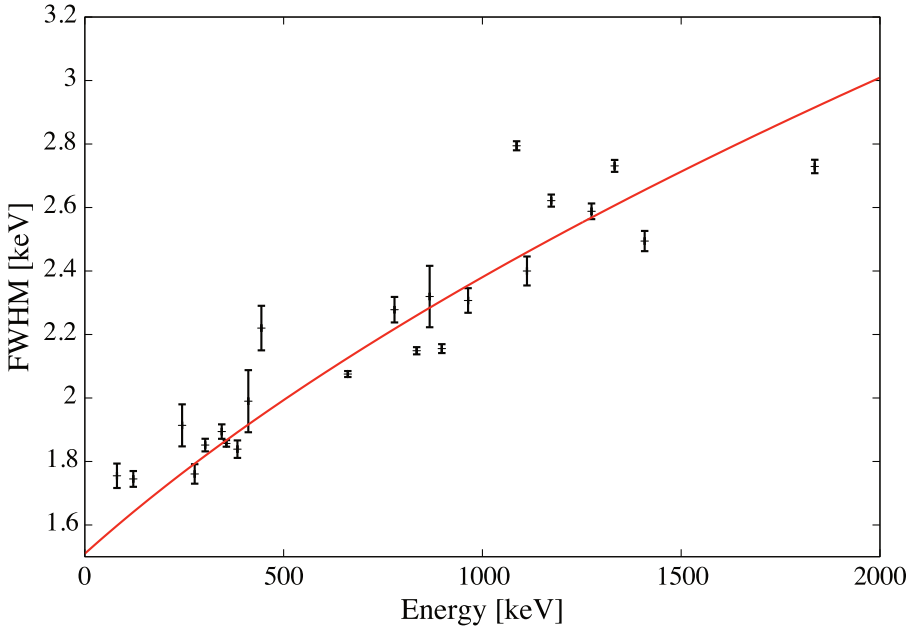

Figure 1.9: FWHM of the peaks as a function of the energy, for detector SC02. The experimental data have been fitted with Eq. 1.1.

The efficiency of germanium detectors highly depends on the energy of the detected γ ray. The absolute photopeak efficiency is defined as

$$\epsilon(E_\gamma) = \frac{I(E_\gamma)}{BR(E_\gamma) \cdot A \cdot \Delta t} \tag{1.2}$$

where $I(E_\gamma)$ is the integral of the photopeak, $BR(E_\gamma)$ is the branching ratio of the transition, A is the activity of the source (reported in Table 1.2) and Δt is the time of the acquisition run.
For an estimation of the efficiency as a function of the energy, two functions had been chosen to fit the experimental data: the Radware function, defined as:

$$ln\epsilon = \left[\left(A + Bln\frac{E}{100keV} + Cln^2\frac{E}{100keV}\right)^{-H} + \left(D + Fln\frac{E}{1MeV} + Gln^2\frac{E}{1MeV}\right)^{-H}\right]^{-\frac{1}{H}} \tag{1.3}$$

where A, B, C, D, F, G, H are the fitting parameters; and the Fazekas function, defined as:

$$ln\epsilon = \sum_{i=1}^{9} c_i \, (lnE)^{i-1} \tag{1.4}$$

with c_i fitting parameters. As can be seen, the Radware function is able to better describe the trend of the experimental points. For this reason, it will be then used in section 2.3 to have an estimation of the efficiency.

1.3. Neutron Wall

The ancillary array Neutron Wall (NW) is formed of 15 pseudohexagonal detector units subdivided into three hermetically separated segments and a pentagonal unit, subdivided into five. Each of these units is filled with Bicron BC501A, a liquid scintillator. NW was coupled to GALILEO, at forward angle with respect to the beam, in order to discriminate between FE reactions, expected to be in coincidence with at least one neutron, and Coulomb-excitation reactions, due to the beam interaction with the ^{181}Ta degrader and the ^{197}Au plunger stopper. This discrimination is done through the analysis of three different parameters, different for neutron and γ-ray events: the Time of Flight, the

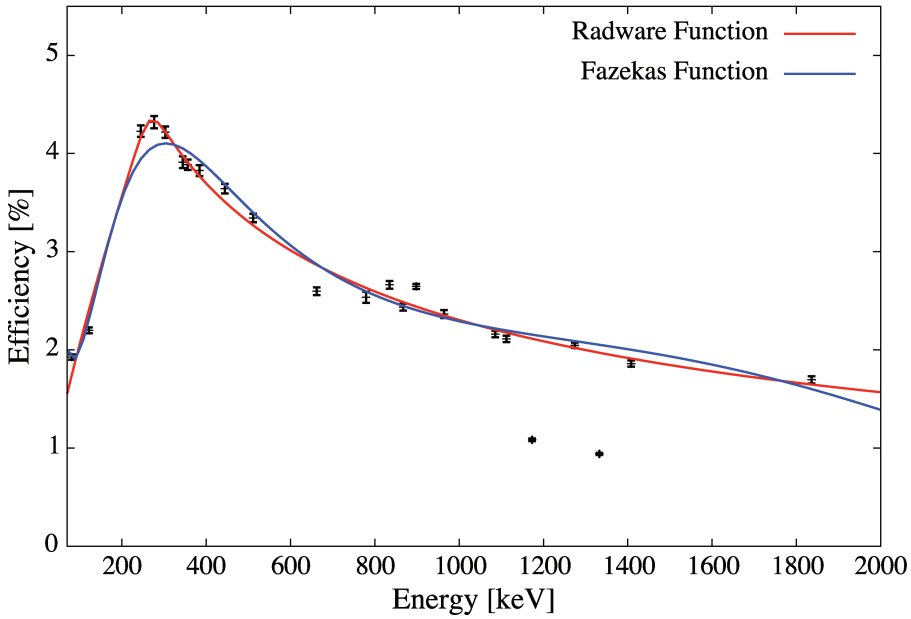

Figure 1.10: Efficiency as a function of energy. The plotted data are the sum of the efficiency of three different HPGe, then multiplied for $\frac{25}{3}$ to have an estimation of the total efficiency of the GALILEO array. The experimental points are fitted with Radware and Fazekas function. The two points that lay below the functions correspond to the energies of the ^{60}Co photo-peaks: this may be due to a wrong value of the measured activity of the source; therefore, these two points were not considered in the fit.

Zero-Cross-Over and the charge-integrated anode signal.
It is thus possible to filter all the events detected, to focus only on FE events, despite a considerable loss in statistics.

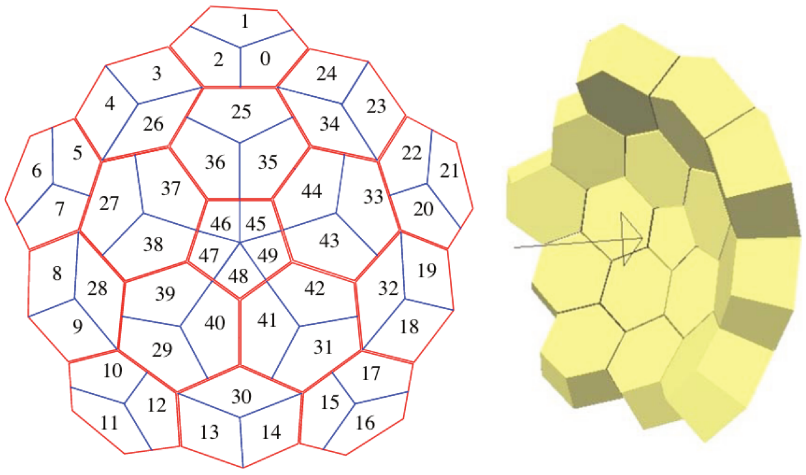

Figure 1.11: The structure of Neutron Wall array. The figure on the left shows a view from down stream. The figure on the right shows a 3D representation of the 16 units of the array. Figure taken from [9].

1.3.1. Neutron gate

During the analysis only the events in coincidence with at least one neutron where considered. This neutron gate was performed using Neutron Wall, and it has the aim to clean the γ-ray energy spectrum and make ^{189}Hg transition peaks more visible, discriminating between FE reaction and other physical phenomena. This also leads to a considerable loss in statistics, as shown in Figure 1.13.

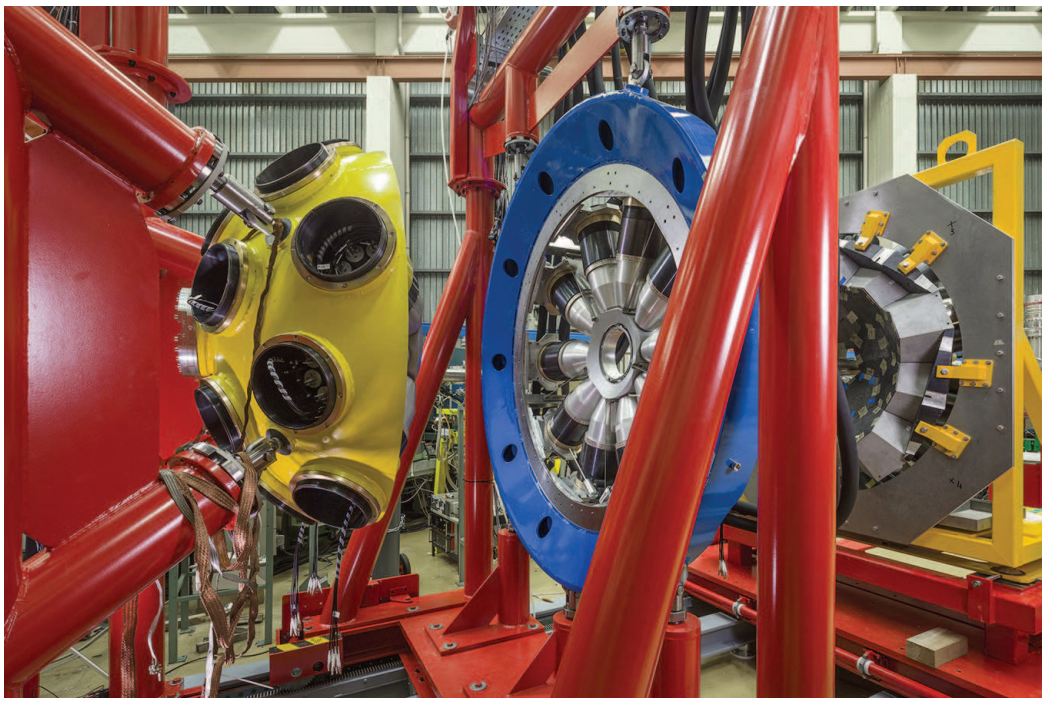

Figure 1.12: A picture of the GALIELO array, on the left, coupled to Neutron Wall, on the right. Figure taken from [8].

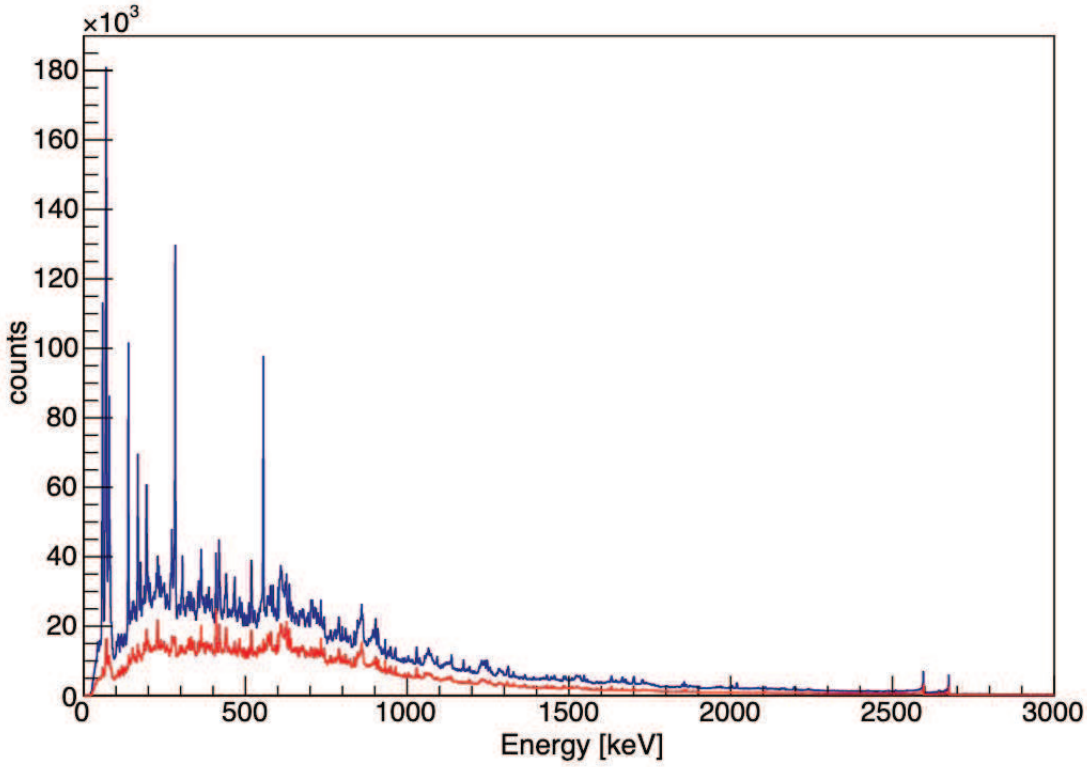

Figure 1.13: Example of a spectrum without the neutron discrimination, in blue, and a spectrum of the events detected in coincidence with at least one neutron, in red. In the latter, the contributions related to other physical phenomena, different from FE reaction, are considerably downsized, and the peaks corresponding to transitions of nuclei produced in FE reactions are more visible, despite a significant loss in statistics.

1.4. The Plunger device

Fundamental for the experiment is the plunger device, developed in collaboration with the Cologne Institute für Kernphysik. This instrument allows direct measurements of lifetime, in a range between picoseconds and nanoseconds. The lifetime measurements of ^{189}Hg were performed via Recoil Distance Doppler Shift method, which will be further discussed in section 2.4.
The used plunger device allows one to vary the distance between the target and the stopper foil, going from few micrometers to some tens of millimeters, with a precision in the sub-micrometer regime. Furthermore, as little material as possible has to be used in the device in order to reach the maximum transparency, still ensuring the needed stability to measure and to maintain constant the distance between the two foils, with a sub-micrometric precision ($\sim$ 40 nm). This high precision can be obtained using the piezoelectric linear slide LPS-24 motor. Lastly, the plunger has to have an active feedback system to compensate for beam induced changes of the target to stopper distance.
The target-stopper distance is measured using the capacitance method: at small distances, the two foils can be approximated to a planar capacitor. The charge collected on the two plates can thus be measured, and the target to stopper distance can be obtained inverting the following formula:

$$Q(x) = C(x)V = \epsilon_0 \epsilon_r \frac{S}{x} V \tag{1.5}$$

where ϵ_0 and ϵ_r are the dielectric constant in vacuum and the relative permeativity, respectively, S is the area of the two foils and V is the amplitude of the voltage signal.

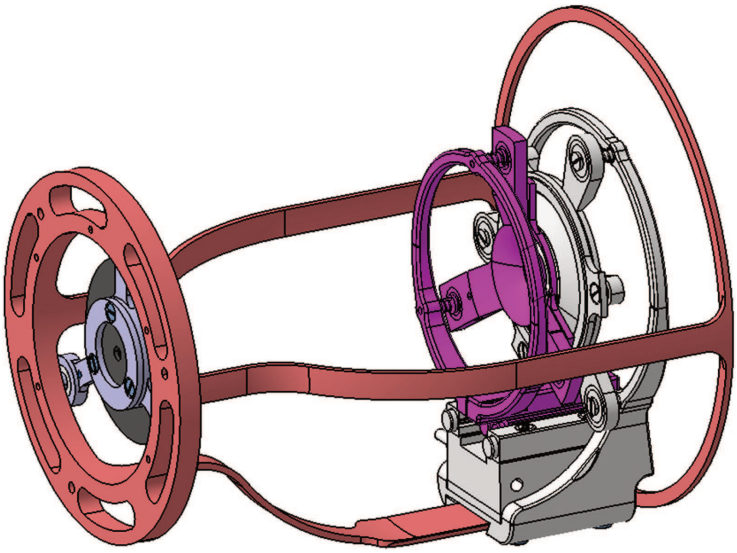

Figure 1.14: A 3D representation of the plunger device. The beam enters from a collimator (4 mm) mounted on its structure, in indigo on the left; it then collides with the target, mounted on its structure, in violet on the right, while the stopper is mounted on its structure, in grey on the right; below, the piezoelectric motor, also in grey. The mechanical support, fixed on the reaction chamber, is in red. Figure taken from [10].

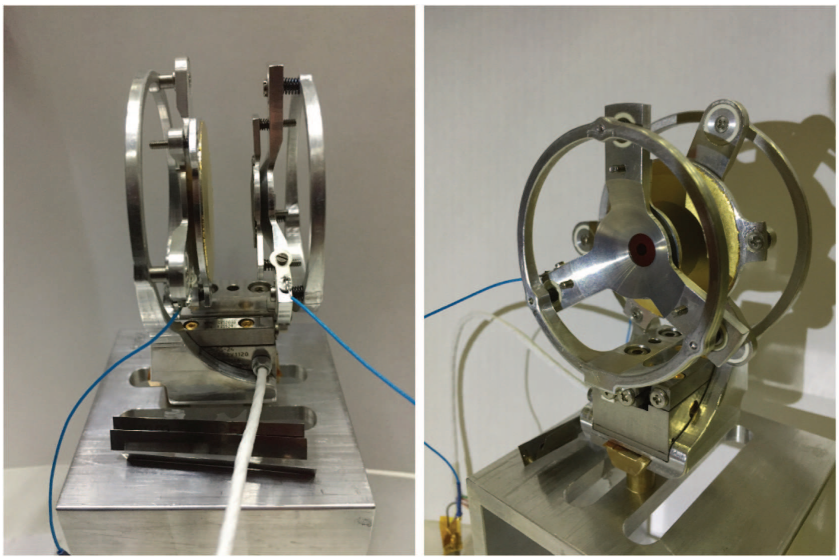

Figure 1.15: Two pictures of the plunger: a side view (on the left) and a front view (on the right). Figure taken from [10].

Analysis and Results

In this chapter the analysis of the data will be explained, and the results of the measurements will be presented. A former measurement of the velocity of the nucleus was performed, in order to Doppler correct the data analysed and to determine the time of flight of the nucleus, as a function of the target to stopper distance; then, an analysis of the spectrum of emission of ^{189}Hg is presented, confronting it with one previously done; after this, the measurement of the lifetime of two excited states, $\frac{17}{2}^+$ and $\frac{21}{2}^+$, was performed; in the end, a discussion of the data analysis is reported, in order to give a theoretical interpretation to the results.

2.1. Determination of the ^{189}Hg velocity

The compound nucleus (CN) created during the FE reaction proceeds in forward direction with respect to the beam. It starts its de-excitation at first by evaporating neutrons (in the case of the nucleus of interest, 5 neutrons). The evaporation residue (ER), ^{189}Hg, then continues its de-excitation by γ decay. The γ ray can be emitted by the ER while it is still in flight, or when it is already at rest in the ^{197}Au stopper foil. The photon emitted in flight will be subject to Doppler shift, according to the equation

$$E_\gamma = E_0 \frac{\sqrt{1-\beta^2}}{1-\beta cos\theta} \tag{2.6}$$

where E_γ is the measured energy of the γ ray emitted in-flight, E_0 is the real energy of the emitted γ ray, β is the ratio between the velocity of the ER in vacuum (the plunger chamber is in vacuum) and the speed of light and θ is the angle of emission of the photon. Because of angular momentum conservation, the ER flies in forward direction at small angles with respect to the beam axis, so θ can be considered with good approximation equal to the angle of the detectors.
In order to perform the Doppler correction (see section 2.4) and to measure the lifetimes of the excited states, it is necessary to measure the velocity β of the ^{189}Hg nucleus. This can be done by evaluating the energy shift between the in-flight peak and the stopped one. From Eq. 2.7, the energy shift is equal to

$$\frac{E_\gamma - E_0}{E_0} \approx \beta cos\theta \tag{2.7}$$

The value of β can be deduced inverting this formula. GALILEO detectors are placed in four rings, three at backwards angles with respect to the beam, so the value of cosθ is negative and the shifted peaks will be at lower energies, and one at 90°, where the Doppler shift will be null.
For the estimation of β, the measurements of the position of the peaks were performed via gaussian fit for the $\frac{17}{2}^+_1 \rightarrow \frac{13}{2}^+_1$ transition, for the three rings and at a target to stopper distance of 200 μm. The results are reported in Table 2.3 and Figure 2.16.
The three measurements are consistent with each other, so the estimation of the velocity is given by the weighted average: β=1.69(7)%.

ring	angle [deg]	β [%]
0	152	1.72(2)
1	129	1.62(1)
2	119	1.81(1)

Table 2.3: Values of the velocity β of ^{189}Hg, measured for the three rings with non-null energy shift.

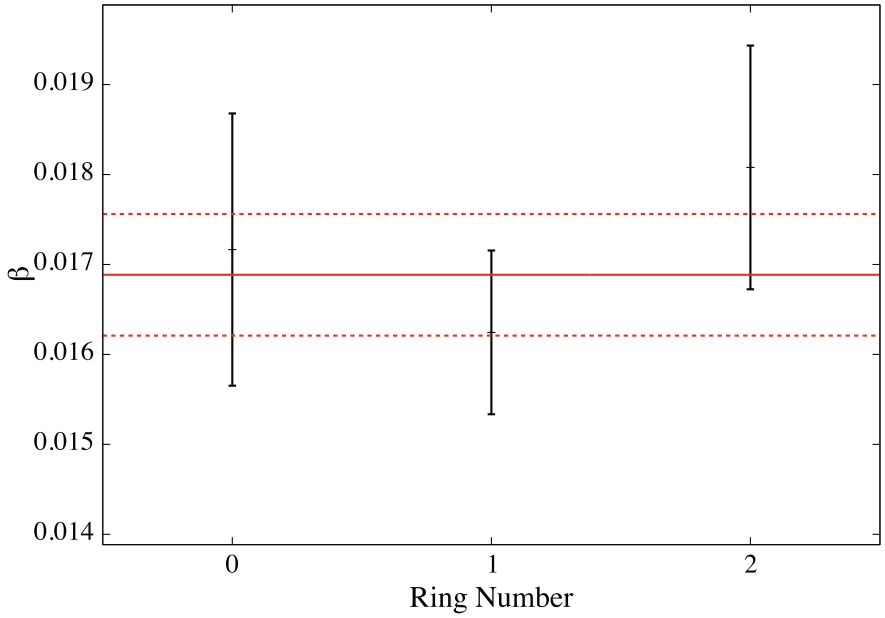

Figure 2.16: Values of β as a function of the number of the ring. The measurements are consistent with each other.

2.2. $\gamma\gamma$-coincidence measurements

As can be seen in Figure 2.19, the decay chain can be very complex to examine, and a single level can have several feeders. The number of nuclei in the state of interest (i) is determined by the following differential equation:

$$\frac{d}{dt}n_i(t) = -\lambda_i \cdot n_i(t) + \sum_{k=i+1}^{N} \lambda_k \cdot n_k(t) \cdot b_{ki} \tag{2.8}$$

where N is the number of the highest feeding level considered, $n_i(t)$ and $n_k(t)$ are the number of nuclei in the levels i and k at time t, λ_j is the decay constant of the levels j (related to the level lifetime by the relation τ_j=1/λ_j) and b_{kj} are the branching ratios from levels k to level j (for every k we have $\sum_j b_{kj} = 1$).
To consider all of the possible known feeders many experimental values, such as feeding intensities and feeding times, have to be determined, which can increase the complexity of the analysis. Further difficulties are caused by the presence of other unknown feeders, which would introduce additional uncertainties [11]. For these reasons, the data analysed were gated on a directly feeding level, in order to examine a single transition at a time. This procedure is called '$\gamma\gamma$-coincidence measurement', and permits to not consider the contributions from other feeders, known or unknown. The differential equation then becomes:

$$\frac{d}{dt}n_i(t) = -\lambda_i \cdot n_i(t) + \lambda_f \cdot n_f(t) \tag{2.9}$$

where f is the only feeder considered. Due to statistical reasons, lifetime measurements performed by gating on a particular feeder have larger experimental error than the ones measured considering all the known potential feeders. Nevertheless, these latter estimations would be affected by systematic errors, caused by incorrect assumptions on the feeders of the level of interest.

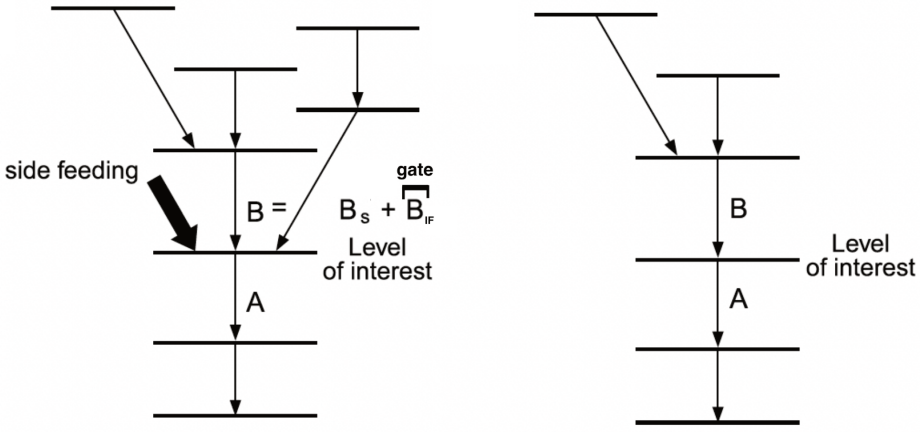

Figure 2.17: Schematic description of the $\gamma\gamma$-coincidence gate. As a consequence of the gating, other side feeders, besides the chosen one, will not be considered. The gate is performed on the in-flight component of the B transition. This procedure significantly simplifies the analysis. Figure adapted from [11].

The data were analysed on *Root*, and were grouped in $TH2$ objects, with the Doppler-corrected (DC) energies on the horizontal axis, and the non-Doppler-corrected (NDC) energies on the vertical axis. The Doppler correction of the energies was performed referring to Eq. 2.7, using the velocity β measured in section 2.7. Referring to Figures 2.17 and 2.18, the gate was performed on the energy corresponding to one of the transitions (B, on the DC axis) right above the transition of interest (A, on the NDC axis). The matrix will show three different components: $\{B_{IF}, A_S\}$, where A is stopped and B is in-flight; $\{B_{IF}, A_{IF}\}$, where both A and B are in-flight; $\{B_S, A_S\}$, where both A and B are stopped. The component $\{B_{IF}, A_S\}$ will not be seen, because it is impossible to have A stopped while B is still in flight. For this reason, the gate is performed only on the components with B_{IF}, in order to not overestimate the number of γ detected for A stopped. A scheme of the procedure can be seen in Figures 2.18.

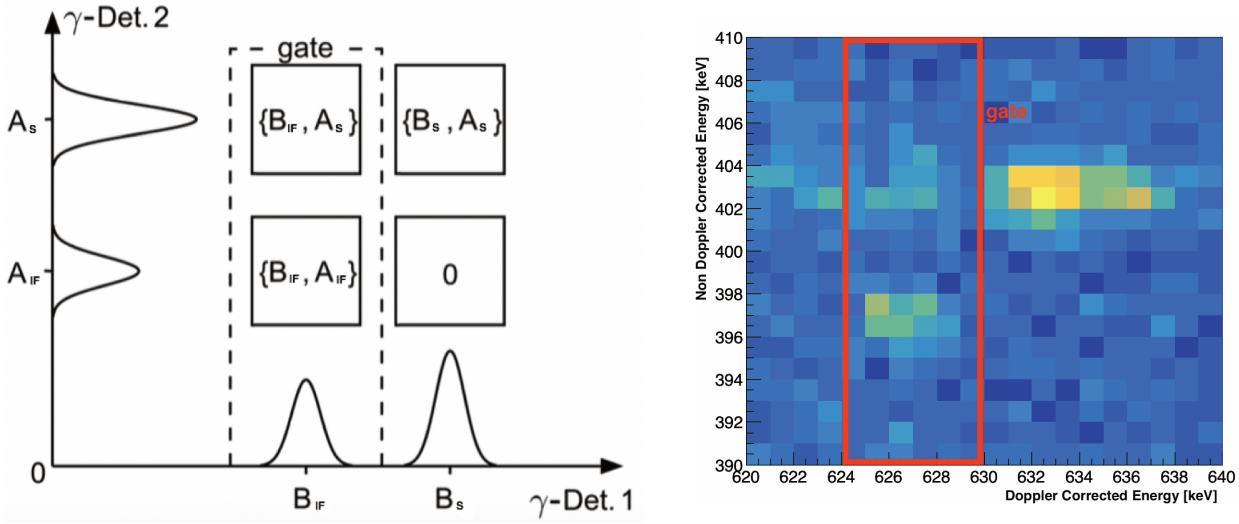

Figure 2.18: On the left, a schematic drawing of the gating on the matrix of data. The gate is performed on the in-flight component of the B transition, in order to not overestimate the A_S component. Figure taken from [6]. On the right, an example of the gating on the matrix of data, performed on the in-flight component of the $\frac{17}{2}^+_1 \rightarrow \frac{13}{2}^+_1$ transition, for Ring 0 at a distance of 300 μm. As can be seen, the $\{B_S, A_S\}$ component is predominant, so an analysis performed without the gating would be affected by a systematic error.

2.3. Spectroscopy

Fusion-evaporation (FE) reactions allow us to populate a wide range of states and bands. Previous analyses of the γ-ray spectrum of ^{189}Hg were performed via FE reactions at Bonn's Institut für Strahlen- und Kernphysik der Universität [12], and with ATLAS, at Argonne National Laboratories [13]. The level scheme proposed by the latter is reported in Figure 2.19.

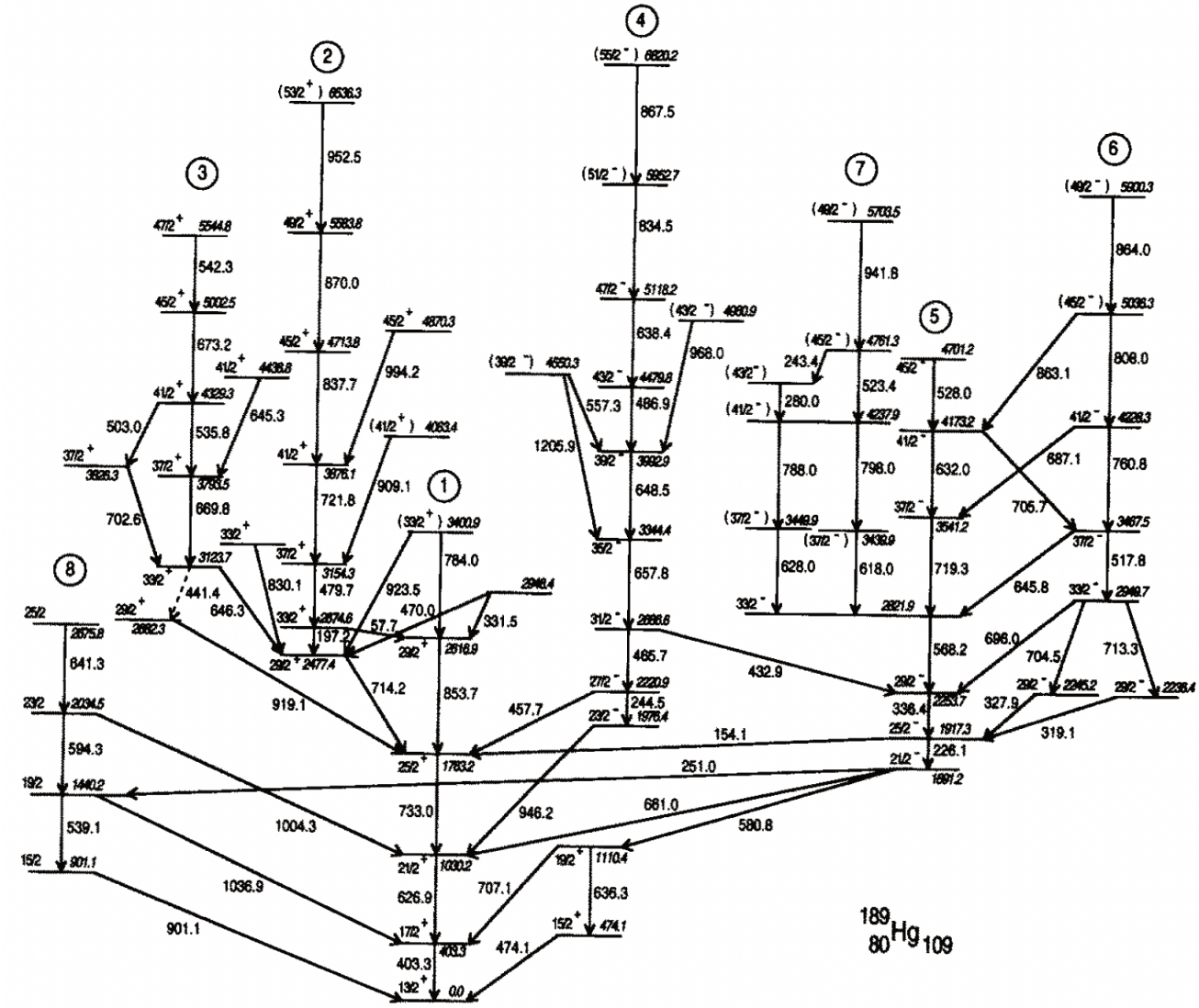

Figure 2.19: Previously proposed level scheme for ^{189}Hg by [13]. Most bands can be understood through cranked shell model calculations. The $\frac{13}{2}^+$ level is not the ground state, but it is an isomer ($T_{1/2}$=8.6(1) m [3]), and its energy is not known. All energies are reported in keV, and are relative to this state. Because the nucleus has been populated from above, the lower-lying levels could not be analysed. Transition and level energies are given in keV.

During this experiment, another analysis of the spectrum was performed, in order to reconstruct the level scheme already known, and also to verify the presence of some unknown feeders, never seen before. Also, no previous lifetime measurements were ever performed on any excited level.
The data from Ring 3 (at 90°, so with null Doppler shift) were analysed with the $\gamma\gamma$-coincidence technique, gating on specific transition energies. The reconstructed spectrum is reported in Figure 2.20.
As can be seen, not all the levels and transition seen in previous experiments are visible, due to the low statistics. Another experiment with a FE transition optimized for ^{189}Hg could be performed in order to obtain a more accurate spectrum reconstruction. Nevertheless, one new band (in red, in Figure 2.20) was observed during the analysis, in coincidence with the $\frac{17}{2}^+_1 \rightarrow \frac{13}{2}^+_1$ transition. Other

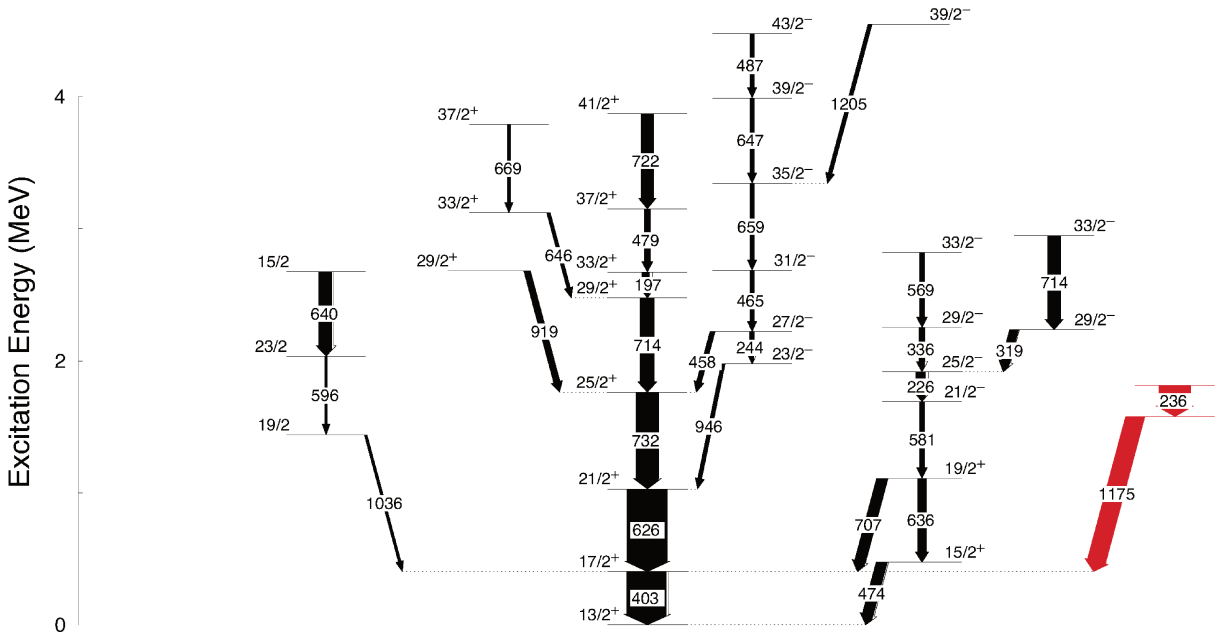

Figure 2.20: Observed level scheme of ^{189}Hg. Most of the bands already known and a new one (in red) were observed. No spin nor parity was assigned to these new levels. Transition and level energies are given in keV. The width of the arrow is proportional to the intensity of the peak corresponding to that transition.

checks were performed on the neighbouring levels, but the new transitions were not observed. For this reason, the hypothesis of a new energy band decaying on the $\frac{17}{2}^+$ seems the more correct. Without having performed any spin or angular distribution experiments, no spin nor parity could be assigned to these levels.

2.4. The RDDS method

The Recoil Distance Doppler Shift (RDDS) method is an experimental technique widely used in nuclear physics for measuring the lifetime of excited states of nuclei in a range going from a few to hundreds of picoseconds.
In FE reactions, the excited states of the CN are populated after the beam impinges on the target. The nucleus leaves the target with a velocity $v = \beta c$ (β measured in section 2.1) and impinges on a ^{197}Au foil. It can emit the photon while still in flight or when already stopped by the foil. The target to stopper distance can be changed in the range of micrometers using the plunger device. The radiation emitted during the flight is subject to Doppler shift, depending on β and on the angle of emission θ. Referring to Eq. 2.7, the Doppler shift is equal to

$$\Delta E = E_\gamma - E_0 \approx E_0 \beta cos\theta \tag{2.10}$$

where E_γ is the energy of the γ ray emitted in-flight, and E_0 is the energy of the emitted γ ray depopulating the level of interest. The spectrum will then show two peaks: one Doppler-shifted, due to the γ-emission during the flight, and one stopped, due to the γ-emission by the evaporation residue at rest in the stopper.
The relative intensity of the in-flight peak (I_{IF}) and the stopped peak (I_S) corresponds to the decay probability during the flight or in the stopper, respectively. The *decay curve* is then defined as:

$$R(t) = \frac{I_S(t)}{I_S(t) + I_{IF}(t)} \tag{2.11}$$

where $I_S(t)$ and $I_{IF}(t)$ are the integrals of the stopped and in-flight peaks, respectively, as a function of the time of flight $t = x/\beta c$, where x is the distance between the target and the stopper [11].

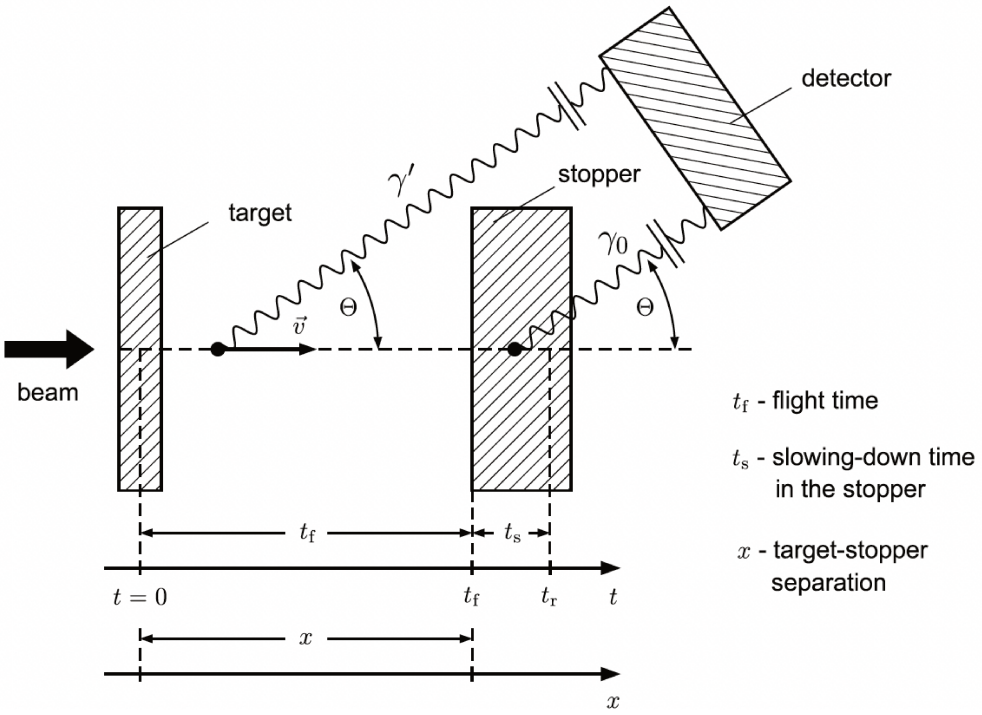

Figure 2.21: Schematic description of the RDDS method. The evaporation residue generated from the fusion-evaporation reaction exits from the target with velocity v. The nucleus can decay during the flight or at rest in the stopper: the γ ray, emitted at angle θ with respect to the beam, is Doppler shifted (γ') or non-Doppler shifted (γ_0), respectively. GALILEO detectors are positioned in four rings at the angles 152°, 129°, 119° and 90°. Figure taken from [11].

2.5. Lifetime measurements and results

At first, for the lifetime measurements, the Decay Curve Method (DCM) had been used. This method consists in measuring the integral of the in-flight (I_{IF}) and stopped (I_S) peaks at different distances (x), and to calculate the *decay curve*, defined in Eq. 2.11. The data will then be fitted with a decreasing exponential:

$$R(t) = Ae^{-t/\tau} + 1 - A \tag{2.12}$$

where $t = \frac{x}{\beta c}$ is the time of flight of the nucleus, A and τ fitting parameters. The parameter τ will then be the estimation of the lifetime of the state of interest.
The DCM does not appear to be the best method for lifetime measurements, for two reasons:

- the level feeding may not have been considered correctly;
- the deorientation of the nucleus[1] was neglected. For instance, there is no universal parameterization for this phenomena.

In general, the fitting function is not known, since the entity of these two contributions are not clear. For this reason, the DCM could be based on invalid assumptions [11]. This method will then not be used for the estimation of τ.
Another widely used technique for lifetime measurement is the Differential Decay Curve Method (DDCM). This method has two great advantages, compared to the DCM: it is not affected by inaccuracy in the estimation of the plunger zero offset, because it depends only on the relative distance between the data points, and the shape of the fitting curve can be chosen arbitrarily, at the only

[1]Nuclear deorientation consists of a randomization or lost of alignment of nuclear spins, usually induced by external factors, such as nuclear reactions. This phenomena affects the nuclear alignment during the flight in vacuum; after the FE reaction in the target, the angular momentum of the CN is usually oriented parallel to the beam axis. During the reaction, the atomic electron configuration are highly distorted, causing a rearrangement of the electrons in more energetically favorable configurations, leading to very high and fast changing magnetic hyperfine fields. This process combines with the decay of the nucleus, leading to a hardly known modification of the *decay curve*.

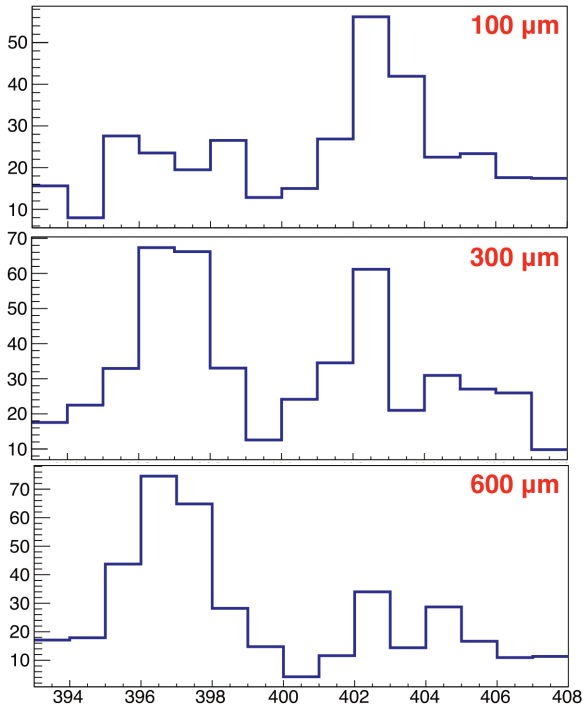

Figure 2.22: Example of the Doppler shift of the peaks at different distances.

condition of being monotone in the region of interest. With the DDCM, the lifetime of the level of interest i can be calculated via

$$\tau_i(x) = -\frac{R_i(x) - \sum_k b_{ki}\alpha_{ki}R_k(x)}{\frac{d}{dx}R_i(x)}\frac{1}{v} \tag{2.13}$$

where b_{ki} and $R_k(x)$ are, respectively, the branching ratio and ratio of the feeding transitions, $\frac{d}{dx}R_i(x)$ is the first derivative of the fitting function, v is the velocity of the CN, and the factor of proportionality α_{ki} is given by

$$\alpha_{ki} = \frac{\omega_k(\Theta)\cdot\epsilon(E_{\gamma k})}{\omega_i(\Theta)\cdot\epsilon(E_{\gamma i})} \tag{2.14}$$

where $\epsilon(E_{\gamma j})$ is the efficiency of the detectors and $\omega_j(\Theta)$ are the angular distributions [11].
In spite of this, the DDCM led to systematical over-estimations of the values of τ_i. The reason for this pattern is the wrong normalization performed in Eq. 2.11. In facts, this normalization does not take into account various factors, such as the time of the acquisition, the intensity of the beam and the state of degradation of the target.
The analysis was thus performed via *Napatau*, a purpose-built software for lifetime estimations, created by the Cologne Institute für Kernphysik. This software tries to overcome these issues by fitting the data not with an exponential function, but with second order exponential splines (a trial was performed also with third order splines, with no significant changes), and then giving a final value for the lifetime, using the DDCM. In the particular case of *Napatau*, the DDCM calculates the k values of the lifetime, where k is the number of points taken into account, via

$$\tau_i = \frac{I_{S,i}}{\frac{d}{dt}I_{IF,i}} \quad i = 1, ..., k \tag{2.15}$$

where $I_{S,i}$ and $I_{IF,i}$ are the integrals of the stopped and in-flight components, respectively, at the $i-th$ distance. The denominator is a time derivative of a measured quantity, and not a direct measurand, and was evaluated by fitting second order exponentials piecewise at the intensities $I_{IF,i}$ measured at every distance. The final estimation for the lifetime will be a weighted average of these values [14].
Napatau takes as an input the values of the distances and the integrals of the in-flight ($I_{IF}(x)$) and stopped ($I_S(x)$) peaks, with the respective errors, and gives as an output the final value of the lifetime,

calculated as explained above, and a graphic of the trend of the residuals, and of the in-flight and stopped components. In order to compare the data at different distances, a normalization of $I_{IF}(x)$ and $I_S(x)$ has to be performed. This normalization has to take in account the time of the acquisition, the intensity of the beam and the state of degradation of the target. For this reason, the normalization was performed over a ^{181}Ta (the fronting of the target) transition coming from the Coulomb excitation of the nuclei. Furthermore, the data points outside the region of sensitivity can be discarded to reduce the systematical error.
An example for the analysis with DCM and DDCM with the wrong normalization will be reported in section 2.5.1, in order to show how the data does not follow a decreasing exponential; then, for the rest of the analysis, only the *Napatau* results will be presented.

2.5.1. Lifetime of the $17/2^+$

For the measurement of the lifetime of the $\frac{17}{2}^+$ state, an energy gate was performed on the transition above ($\frac{21}{2}^+ \rightarrow \frac{17}{2}^+$), and I_{IF} and I_S where measured only for Ring 0 and Ring 2: the data for Ring 1 were not sufficiently good. In order to highlight the peaks of the transition of interest, a subtraction of the background was performed.
As mentioned above, the DCM was not the optimal method for measuring lifetimes, and the first attempt for DDCM had to be corrected with a different normalization. In support of this thesis, the *decay curve* and the values for τ_i (calculated as Eq. 2.13) of $\frac{21}{2}^+ \rightarrow \frac{17}{2}^+$ measured for Ring 1 is reported in Figure 2.23.

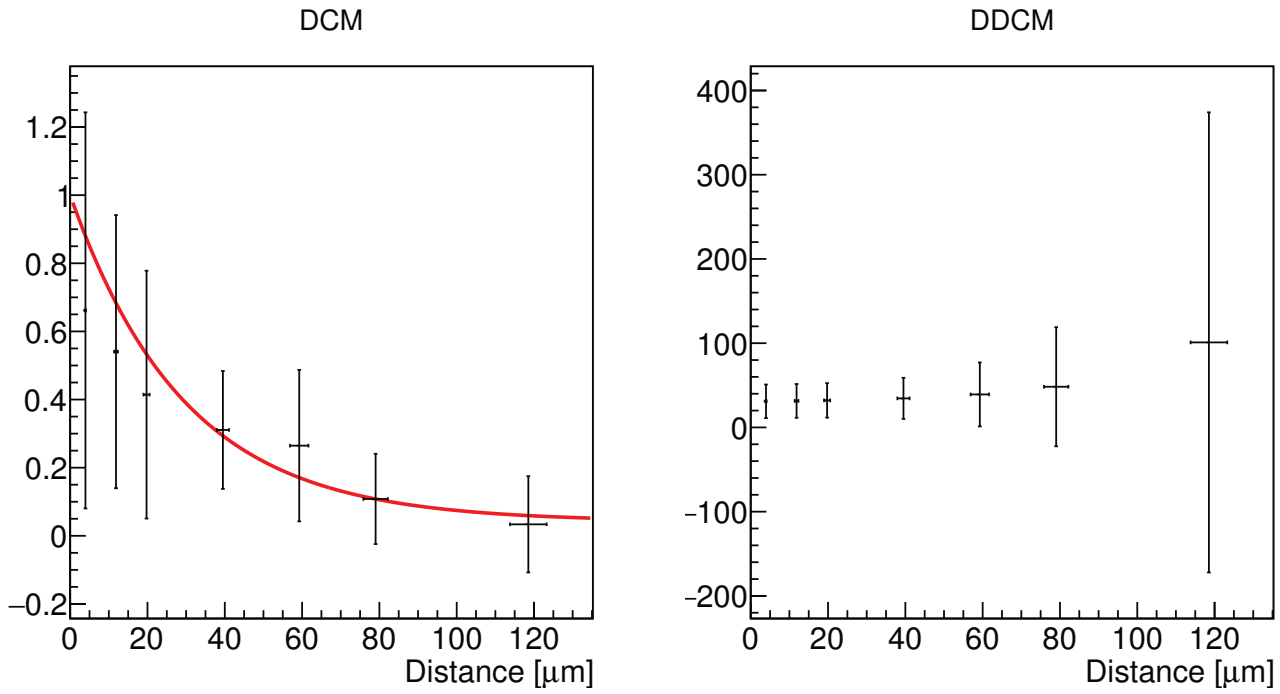

Figure 2.23: DCM and DDCM (with the wrong normalization used in 2.11) of $\frac{21}{2}^+ \rightarrow \frac{17}{2}^+$ measured for Ring 1. In the first, it is clear that the data points does not follow the exponential fitting function: for this reason, we will not use the DCM for lifetime estimations; in the latter, a systematic pattern is evident: for this reason, the normalization has to be changed.

It is clear that these two methods are not appropriate to calculate the lifetime of the state. In order to be exhaustive, the lifetime measured with these two methods are

$$\tau^{DCM}_{21/2^+} = 30 \pm 20\ ps \qquad \tau^{DDCM}_{21/2^+} = 30 \pm 14\ ps$$

From now on, only the results calculated via *Napatau* will be presented. The values of the lifetime estimates given by *Napatau* are reported in Table 2.4.

Ring	τ [ps]
0	40 ± 9
1	–
2	30 ± 20

Table 2.4: Values of the lifetimes of the $\frac{17}{2}^+$ calculated via *Napatau*, for Ring 0 and Ring 2. No results are presented for Ring 1 because the data were of poor quality.

The analysis performed for the $\frac{17}{2}^+$ level is reported in Figure 2.24.

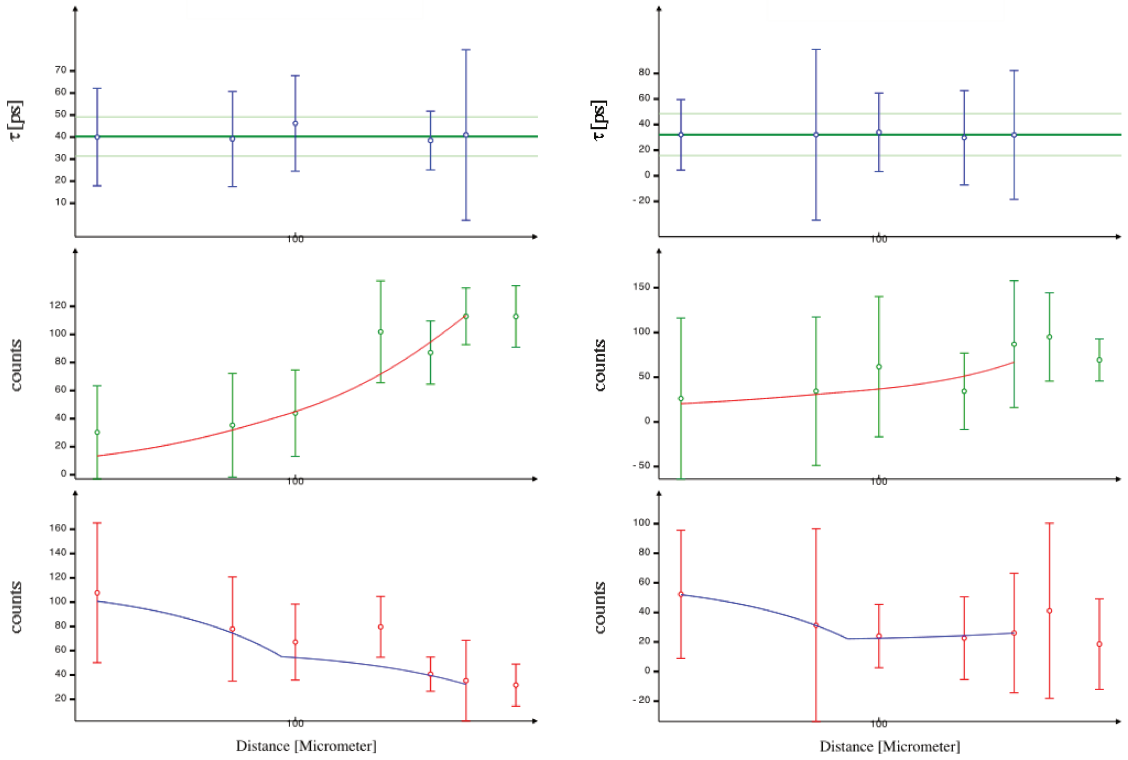

Figure 2.24: On the left, the results given by *Napatau* for Ring 0; on the right, the ones for Ring 2 for the $\frac{17}{2}^+$ state. No results are presented for Ring 1 because the data were of poor quality. From top to bottom: the analysis of the residues, which are evenly distributed, and the trends of I_{IF} and I_S, normalized as mentioned in section 2.5. As can be seen, in both cases the residuals have a random pattern.

The results are consistent with each other, so a final estimation of the lifetime of the $\frac{17}{2}^+$ state is given by the weighted average:

$$\tau_{17/2^+} = 38 \pm 8 \; ps$$

2.5.2. Lifetime of the $21/2^+$

For the measurement of the lifetime of the $\frac{21}{2}^+$ state, an energy gate was performed on the transition above ($\frac{25}{2}^+ \rightarrow \frac{21}{2}^+$), and I_{IF} and I_S where measured only for Ring 0 and Ring 1: the data for Ring 2 were not sufficiently good. In order to highlight the peaks of the transition of interest, a subtraction of the background was performed.
The values of the lifetime estimates given by *Napatau* are reported in Table 2.5.
The analysis performed for the $\frac{21}{2}^+$ level is reported in Figure 2.25.
The results are consistent with each other, so a final estimation of the lifetime of the $\frac{21}{2}^+$ state is given by the weighted average:

$$\tau_{21/2^+} = 29 \pm 5 \; ps$$

Ring	τ [ps]
0	27 ± 5
1	40 ± 10
2	–

Table 2.5: Values of the lifetimes of the $\frac{21}{2}^+$ state calculated via *Napatau*, for Ring 0 and Ring 1. No results are presented for Ring 2 because the data were of poor quality.

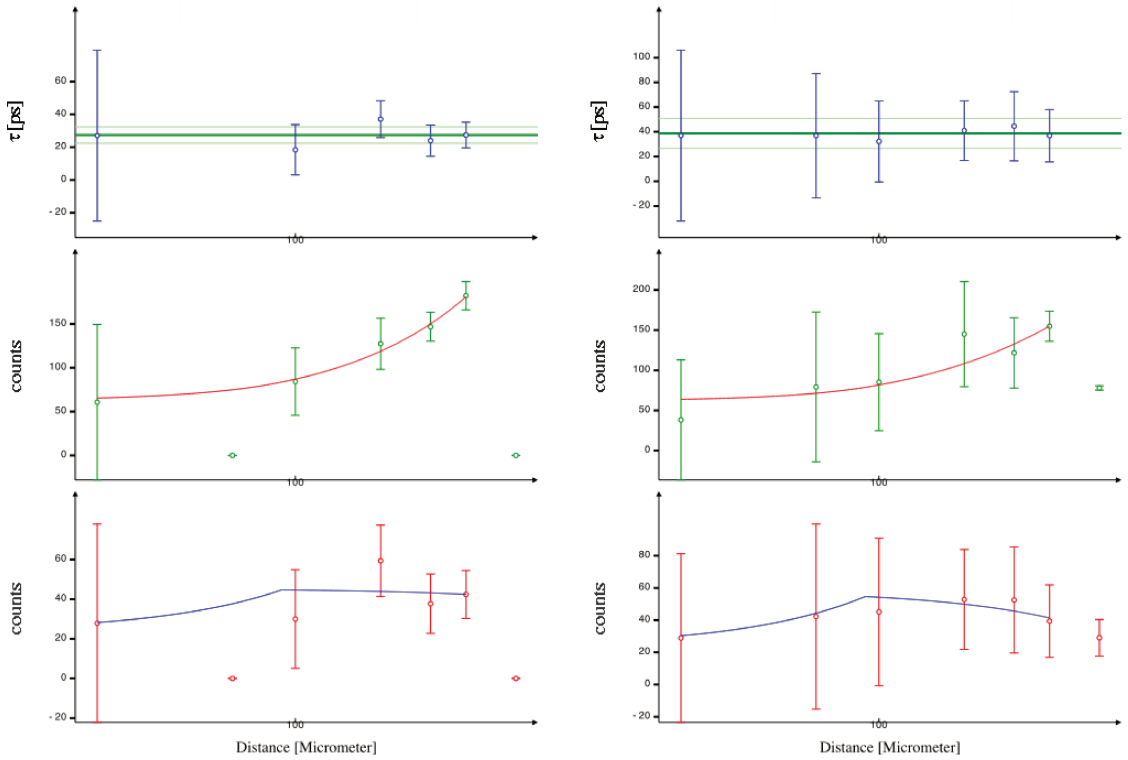

Figure 2.25: On the left, the results given by *Napatau* for Ring 0, on the right, the ones for Ring 1 for the $\frac{21}{2}^+$ state. No results are presented for Ring 2 because the data were of poor quality. From top to bottom: the analysis of the residues, which are evenly distributed, and the trends of I_{IF} and I_S, normalized as mentioned in section 2.5. As can be seen, in both cases the residuals have a random pattern.

2.6. Discussion of the results

The two transitions analysed are $\frac{17}{2}^+ \rightarrow \frac{13}{2}^+$ and $\frac{21}{2}^+ \rightarrow \frac{17}{2}^+$. The type of the transition and its multipolarity are given by the rules of composition of angular momentum:

$$|I_i - I_f| \leq L \leq |I_i + I_f| \tag{2.16}$$

where I_i and I_f are the angular momentum of the initial and final state, respectively; and by the conservation of parity:

$$\pi(EL) = (-1)^L \qquad \pi(ML) = (-1)^{L+1} \tag{2.17}$$

It is thus clear that the only permitted transitions are: $E2$, $M3$, $E4$ and $M5$. Knowing that $E2$ are the most probable transitions, with respect to the other permitted, we assume that the two transition analysed are predominantly $E2$. We can measure the probability of transition with the following equation:

$$\lambda(EL) = \frac{8\pi(L+1)}{L\left[(2L+1)!!\right]^2} \frac{e^2}{4\pi\epsilon_0\hbar c} \left(\frac{E_\gamma}{\hbar c}\right)^{2L+1} \left(\frac{3}{L+3}\right)^2 cR^{2L} \tag{2.18}$$

where E_γ is the energy of the transition measured in MeV and $R = r_0 A^{\frac{1}{3}}$ is the radius of the nucleus, with r_0=1.2 fm and A the atomic mass. We can define the reduced probability of transition as [15]:

$$B(\sigma L) = \frac{|\langle\psi_f| O(\sigma L) |\psi_i\rangle|^2}{2I_i + 1} \tag{2.19}$$

where ψ_i and ψ_f are the wave function of the initial and final state, respectively, $O(\sigma L)$ is the multipole operator (in the case of $E2$ transitions: $O(E2) = Ze(3z^2 - r^2)$, where Z is the atomic number, e is the elementary charge, z and r are the third cartesian coordinate and the radial coordinate, respectively), and I_i is the angular momentum of the initial state of the transition. Approximate estimates for the reduced probability of transition, assuming that every transition involves only one nucleon (single particle transitions), are given by the Weisskopf estimates:

$$B_{sp}(EL) = \frac{1}{4\pi}\left(\frac{3}{L+3}\right)^2 r_0^{2L} A^{\frac{2L}{3}} \quad e^2 fm^4 \tag{2.20}$$

For $E2$ transition, it can be proven that the experimental reduced probability transition is equal to

$$B(E2) = \frac{BR_\gamma}{\tau \cdot E_\gamma^5 \ (1+\alpha) \cdot 1.223 \times 10^9} \quad e^2 fm^4 \tag{2.21}$$

where BR_γ is the branching ratio of the transition (both in the case of $\frac{17}{2}^+$ and $\frac{21}{2}^+$ is equal to 1, because they decay only in one possible way), τ is the measured lifetime for the state, E_γ is the energy of the γ ray measured in MeV, α is the internal conversion coefficient (calculated via [16]) and the factor 1.223×10^9 contains all the constants of Eq. 2.18.
The experimental reduced probability of transition expressed in Weisskopf units, given by

$$B_{W.u.}(E2) = \frac{B(E2)}{B_{sp}(E2)} \quad W.u. \tag{2.22}$$

gives us information on the collective behaviour of the transition: if the value is near or below the unit, the single particle transition is a good approximation; the farther it is from the unit, the more the transition is collective. The single particle and the experimental reduced probability of transition and its value expressed in $W.u.$, are reported in Table 2.6.

	$B_{sp}(E2)$ $[e^2fm^4]$	$B(E2)$ $[e^2fm^4]$	$B_{W.u.}(E2)$ $[W.u.]$
$\frac{17}{2}^+ \rightarrow \frac{13}{2}^+$	64	1900 ± 400	30 ± 6
$\frac{21}{2}^+ \rightarrow \frac{17}{2}^+$	64	290 ± 50	4 ± 1

Table 2.6: Values of the Weisskopf estimates, the experimental reduced probability transition and the number of Weisskopf units per transition.

The $\frac{17}{2}^+$ level presents a value for $B_{W.u.}(E2)$ far from the unit, compatible with the hypothesis of a collective behaviour. This was to be expected, both because it is a typical behaviour for mid-shell nuclei (not near to any magical nucleus), and because it is a behaviour manifested also in the neighbouring nuclei [1, 17]. On the other hand, it is unclear what the nature of the $\frac{21}{2}^+$ is. The values of the $B_{W.u.}(E2)$ of the first two excited states, 2^+ and 4^+, for ^{188}Hg are increasing (respectively, 44 ± 2 and 92 ± 38), while for ^{190}Hg are decreasing (respectively, 45 ± 3 and 19 ± 16). The $B(E2; J+4 \rightarrow J+2)/B(E2; J+2 \rightarrow J)$ ratio for ^{189}Hg is lower than one, a behaviour more similar to the trend of heavier even-even nuclei, such as ^{190}Hg, and different from the trend of lighter nuclei, such as ^{188}Hg. Despite this, the low value of the $B_{W.u.}(E2)$ for the second excited state, namely $\frac{21}{2}^+$, with respect to the 4^+ states of the heavier even-even nuclei may suggest that this state does not follow the same trend. Further investigations could bring to brighter conclusions on the nature of this state.

Conclusions

The aim of this thesis was to study some of the spectroscopic properties of ^{189}Hg, such as the reconstruction of the spectrum of emission of the nucleus, and to measure the lifetime of two excited states. The experiment was performed at Laboratori Nazionali di Legnaro in 2016, firstly focused on the study of ^{188}Hg, populated via fusion-evaporation reaction, with a ^{34}S beam impinging onto a ^{160}Gd target. The second most populated nucleus during the reaction was ^{189}Hg, of interest for this thesis.
The Neutron Wall array, used to discriminate between fusion-evaporation reactions and other phenomena not of interest, was coupled to the GALILEO array, used to perform the γ-ray detection. For the latter, a presorting of the data was performed, with a particular focus on the energy calibration and on the study of resolution and efficiency as a function of the energy.
The spectroscopic analysis has revealed most of the bands already known, but not all levels and transitions were observed. Also, a new band was observed, but no spin nor parity could be assigned to these levels.
The Recoil Distance Doppler Shift method was used for lifetime measurements, with the $\gamma\gamma$-coincidence technique. A first attempt was done via *Decay Curve Method*, leading to incorrect conclusions. Then, the analysis was performed via *Napatau*, a purpose-built software for lifetime analysis via *Differential Decay Curve Method*. The two states of interest were $\frac{17}{2}^+$ and $\frac{21}{2}^+$, and the respective lifetimes are reported below:

$$\tau_{17/2^+} = 38 \pm 8\ ps \qquad \tau_{21/2^+} = 29 \pm 5\ ps \tag{3.23}$$

Finally, the reduced probabilities of transition were calculated, assuming the two transitions to be $E2$, and were compared to the respective Weisskopf estimates. From that, we can conclude that the $\frac{17}{2}^+$ level present a collective behaviour, while for the $\frac{21}{2}^+$ further investigations are needed to make conclusions.
In conclusion, additional estimations for lifetimes of ^{189}Hg could be performed in future experiments by optimizing the initial reaction for this type of nucleus, in order to improve the statistics. This operation would lead to more accurate values of the lifetimes with lower errors, and would allow us to extend the study to other states. Furthermore, other experiments could be conducted with the same techniques, in order to study lighter even-odd nuclei, also of great interest.

Bibliography

[1] M. Siciliano, I. Zanon, and A. Goasduff et al. "Shape coexistence in neutron-deficient ^{188}Hg investigated via lifetime measurements". In: *Physical Review C* 102 (2020).

[2] F. Hannachi et al. "High-spin excitations of $^{187,188}Hg$". In: *Nuclear Physics* A481 (1988), pp. 135–160.

[3] *National Nuclear Data Center website.*

[4] B.A. Marsh et al. "Characterization of the shape-staggering effect in mercury nuclei". In: *Nature Physics* 14 (2018), pp. 1063–1067.

[5] I. Angeli and K.P. Marinova. "Table of experimental nuclear ground state charge radii: An update". In: *Atomic Data and Nuclear Data Tables* 99 (2013), pp. 69–95.

[6] Irene Zanon. "Study of Shape Coexistence in the ^{188}Hg nucleus via lifetime measurements". Università degli Studi di Padova, 2018.

[7] *Istituto Nazionale di Fisica Nucleare webpage.*

[8] *Laboratori Nazionali di Legnaro webpage.*

[9] J. Ljungvall, M. Palacz, and J. Nyberg. "Monte Carlo simulations of the Neutron Wall detector system". In: *Nuclear Instruments and Methods in Physics Research A* 528 (2004), pp. 741–762.

[10] C. Müller-Gatermann, F. von Spee, and A. Goasduff et al. "A new dedicated plunger device for the GALILEO γ-ray detector array". In: *Nuclear Inst. and Methods in Physics Research A* 920 (2019), pp. 95–99.

[11] A. Dewald, O. Möller, and P. Petkov. "Developing the Recoil Distance Doppler-Shift technique towards a versatile tool for lifetime measurements of excited nuclear states". In: *Progress in Particle and Nuclear Physics* 67 (2012), pp. 786–839.

[12] M. Guttormsen et al. "Rotation Aligned Bands and Configuration Dependent Interaction in ^{189}Hg". In: *Physical Review C* 100 (2019).

[13] I.G. Bearden, R.V.F. Janssens, and M.P. Carpenter et al. "Detailed band structures in ^{189}Hg and ^{190}Hg". In: *Nulcear Physics A* 576 (1994), pp. 441–476.

[14] B. Saha. "Napatau or Tk-Lifetime-Analysis - Institute for Nuclear Physics". In: (2003).

[15] P.J. Brussaard and P.W.M. Glaudemans. *Shell-model applications in nuclear spectroscopy.* North-Holland Publishing Company, 1977.

[16] *BrIcc conversion coefficient calculator.*

[17] B. Olaizola, A.B. Garnsworthy, and F.A. Ali et al. "Shape coexistence in the neutron-deficient lead region: A systematic study of lifetimes in the even-even $^{188-200}$Hg with the GRIFFIN spectrometer at TRIUMF". In: *Physical Review C* 100 (2019).

[18] A. Goasduff, D. Mengoni, and F. Recchia et al. "The GALILEO γ-ray array at the Legnaro National Laboratories". In: *Nuclear Inst. and Methods in Physics Research A* 1015 (2021).

[19] J. Bradbury, D. Testov, and S. Bakes et al. "Lifetime measurements using a plunger device and the EUCLIDES Si array at the GALILEO γ-ray spectrometer". In: *Nuclear Inst. and Methods in Physics Research A* 979 (2020).

[20] Ö. Skeppstedt, H.A. Roth, and L. Lindström et al. "The EUROBALL neutron wall - design and performance tests of neutron detectors". In: *Nuclear Inst. and Methods in Physics Research A* 421 (1999), pp. 531–541.

[21] A. Esmaylzadeh et al. "Lifetime determination in ^{190,192,194,196}Hg via $\gamma - \gamma$ fast-timing spectroscopy". In: *Physical Review C* 98 (2018), p. 14313.